UNIVERSITÀ DI PARMA
ARCHIVIO DELLA RICERCA

University of Parma Research Repository

Burial stylolites enhance karst dissolution and control cave geometry in heterolithic carbonates, Salitre Formation, Brazil

note finali coverpage

(Article begins on next page)

12 August 2025

Graphical abstract:

Bedding-parallel stylolites in dolomitic limestone consist of high-porosity (up to 20%) mm- to cm-thick zones, which acted as potential fluid conduits.
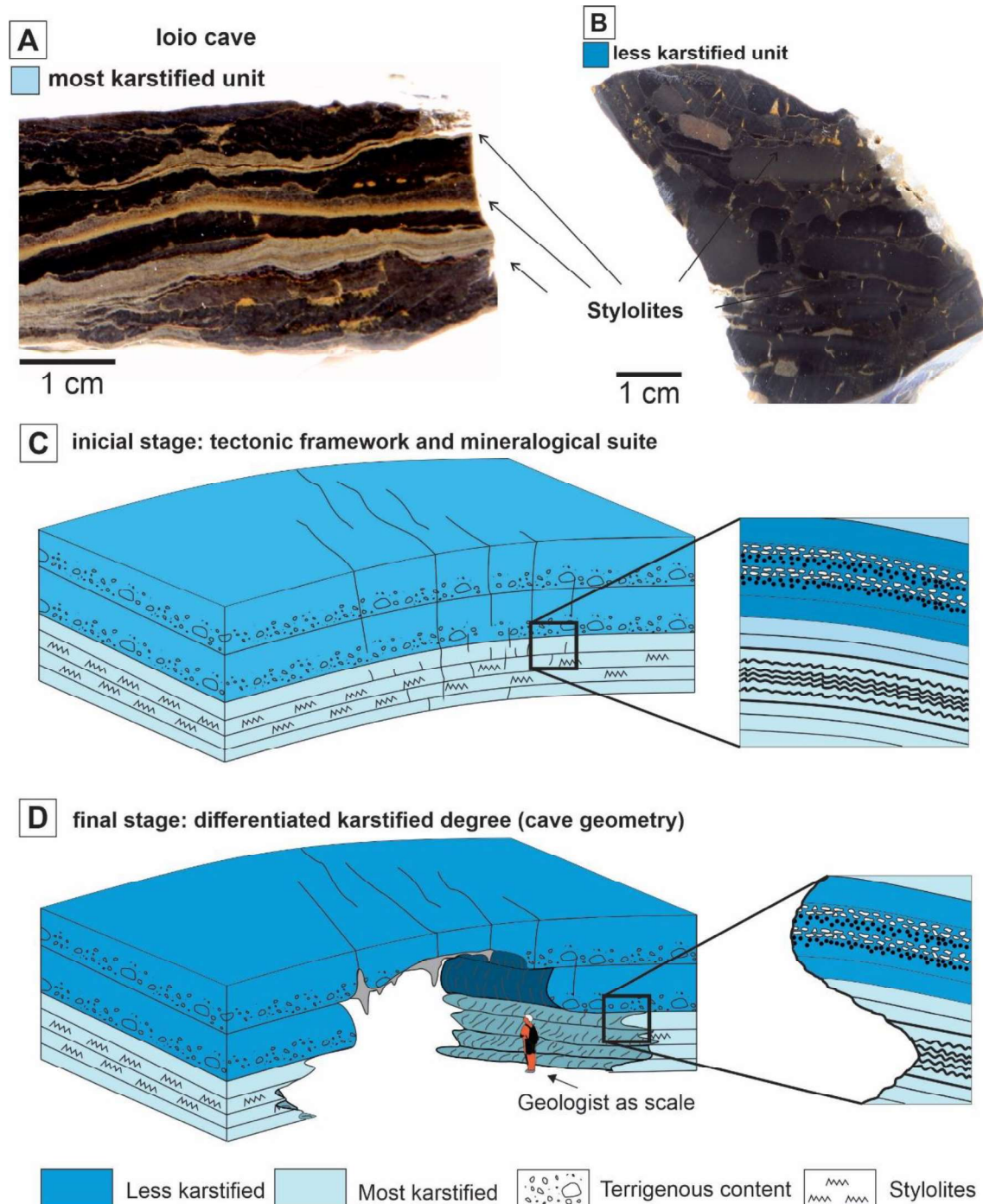
(A) Representative sample from the most karstified unit with clusters of stylolites. (B) Representative sample from the less karstified unit with submillimetre stylolites. (C) 3D model from the inicial stage of cave development. (D) Final stage of cave geometry development.

Highlights:

- Beds dissolution intensity is estimated from 2D vertical cave profiles

- Dissolution intensity does not depends on host rock petrophysical properties

- Spacing and thickness of burial stylolites control bed dissolution intensity

- Burial stylolites have 20% porosity and consist of detrital dolomite grains

- 2D cave geometry depends on stylolites attributes acting as flow pathways

Burial stylolites enhance karst dissolution and control cave geometry in heterolithic carbonates, Salitre Formation, Brazil

Cayo C. Cortez Pontes[a*], Fabrizio Balsamo[b], Mattia Pizzati[b], Francisco H. Bezerra[a], Vincenzo La Bruna[a], Rebeca S. Lima[a].

[a] Programa de Pós-Graduação em Geodinâmica e Geofísica, Universidade Federal do Rio Grande do Norte, Natal, RN, Brazil

[b] Dipartimento di Scienze Chimiche, della Vita e della Sostenibilità Ambientale, Università di Parma, Italy

Abstract

Understanding the karstification process in fractured carbonates is a key factor in developing and exploiting fractured and karstified reservoirs. This study documents the relationship among the 2D geometry, stratigraphy and petrophysical properties of a cave system developed in a Neoproterozoic mixed carbonate-siliciclastic sequence. We applied a multidisciplinary and multiscale approach that combines structural geological surveys, cave imaging by Laser Detecting and Ranging (LiDAR), linear scanlines, stratigraphic logs, uniaxial compressive strength (UCS) and mercury-intrusion porosimetry and 2D image analysis. We found that bedding-parallel stylolites in dolomitic limestone consist of high-porosity (up to 20%) mm- to cm-thick zones, which acted as potential fluid conduits. Thin section analyses showed that beds with closely spaced and thicker stylolites are more karstified and dissolved than beds with greater spacing or the absence of stylolites, indicating that stylolitic zones act as flow pathways in low porosity-permeability carbonates. The petrophysical properties of primary porosity, pore size distribution, density and capillary pressure have no direct relationship with karstification intensity. We conclude that burial

stylolite clusters may control the hypogenic cave geometry. These findings could have implications for fluid flow and ore deposits associated with reactivated stylolites.

Keywords: Carbonate reservoir; Karst; Stylolites; Hypogene cave; Fluid flow; Salitre formation.

1 Introduction

Karst features include different high-porosity structures spanning from the macroscale, with cave systems of kilometers of conduits, to the microscale, as vugs a few millimeters in size. They can occur at different depths and are mainly related to the chemical dissolution of carbonate sequences (Flugel, 2010). The comprehensive understanding of karstification of carbonate units is fundamental to the development and exploitation of hydrocarbon reservoirs, bedrock quality assessment in anthropic areas, and hydrogeological behavior of aquifers (Heward et al., 2000; Klimchouk et al., 2000; Petrella et al., 2007). Understanding the geometry and size of karst porosity is a key factor for the simulation of fluid flow in reservoirs, with direct application to the oil industry and carbonate aquifers (Popov et al., 2007; Agar and Geiger, 2015; Gholpoiur et al., 2016; Xu et al., 2017; Lyu et al., 2020). In oil reservoirs, the growth of macroscopic porosity (e.g., increase in volume available for fluid accommodation) and permeability (e.g., fluid flow capacity) is associated with karstification (Araújo et al., 2021; Klimchouk et al., 2000; Worthington and Ford, 1995).

Karst systems can be classified by evaluating the nature of the fluids responsible for their formation. Surficial fluids enriched in CO_2 flowing downward by gravity give rise to

epigene karst (Audra and Palmer, 2011; Pisani et al., 2022). In contrast, when karst is formed by an ascending, relatively deep hydrothermal or sulfate-enriched fluid flow (Dublyansky, 2012; Palmer, 2016), it results in hypogene karst (Klimchouk, 2007). Hypogene karst systems comprise interconnected vugs and caves with a wide range of sizes and volumes (Flugel, 2010).

Hypogenic karst systems are developed by undersaturated water with respect to the country rock and are formed by ascending fluid flow (Dreybrodt, 1990; Klimchouk et al., 2000). These systems are mainly controlled by macroscale structural and sedimentary discontinuities (e.g., fractures and bedding planes), stratigraphic (e.g., type of rock) and hydrological settings (e.g., De Waele et al., 2009; Ennes-Silva et al., 2016; Cazarin et al., 2019; Balsamo et al., 2020). Other important intrinsic factors influencing hypogene karst development are related to the lithology (e.g., mineralogy, fabric and texture) and petrophysical properties (e.g., porosity and permeability) of the host rock.

Previous studies highlighted the relevance of fracture network persistence and density in the development of hypogenic cave systems in gently folded carbonate sequences (Antonellini et al., 2019; Ogata et al., 2014; Palmer, 1991, 1989; Pisani et al., 2021; Pontes et al., 2020; Wang et al., 2017). The time-space evolution of fractures influences the generation and evolution of karst systems (Araújo et al., 2021; Auler et al., 2017; Barbier et al., 2012; Ennes-Silva et al., 2016; La Bruna et al., 2021; Lamarche et al., 2012; Laubach et al., 2009). Fracturing and diagenesis influence the development of karst systems on a regional and mesoscale, generating preferential pathways for fluid flow (Antonellini et al., 2019; Bagni et al., 2020; Pisani et al., 2019; Wang et al., 2017).

Another important feature that must be observed, principally in carbonate reservoirs, is the stylolites. Stylolites are wavy diagenetic features caused by pressure dissolution that occur initially at the grain-crystal interface at the micron scale. They are filled with insoluble materials such as clay minerals, organic matter, and sulfides (Hosseini et al., 2022 and

3

references therein) and can be classified into burial and tectonic types based on their formation mechanism and orientation with respect to bedding. Burial stylolites develop parallel to bedding due to lithostatic pressure, while tectonic stylolites usually develop at high angles with respect to bedding and form due to compressional tectonic stresses.

Stylolites acting as potential conduits for flow have been described in recent decades (Araújo et al., 2021; Bruna et al., 2019; Hosseini et al., 2022; Rustichelli et al., 2015) but are generally considered impermeable, acting as barriers to flow (Gomez-Rivas et al., 2022). Therefore, stylolites require special attention in carbonate reservoirs due to their potential impact on mechanical strength, diagenetic processes, dolomitization, ore deposits and fluid flow (Baud et al., 2016; Bruna et al., 2019; Gomez-Rivas et al., 2022; Heap et al., 2014; Hosseini et al., 2022), but little has been quantified related to karst systems.

This work adopted a multidisciplinary and multiscale approach to document how layer properties (bed thickness, petrophysical properties, attributes of bedding-parallel stylolites) control hypogenic karst dissolution intensity in the heterolithic tight carbonates of the Salitre Formation, Brazil. We selected two karst systems named Ioio cave and Torrinha cave, which occur in the southern portion of the Irece basin (Fig. 1). We combine structural geological surveys with cave imaging by Laser Detecting and Ranging (LiDAR), linear scanlines, stratigraphic logs into caves, uniaxial compressive strength (UCS) measured with the Schmidt hammer, mercury-intrusion porosimetry and 2D image analysis (total porosity and pore-size distribution), thin section observations, scanning electron microscopy (SEM) and energy dispersive X-ray spectrometry (EDS) analysis. This hypogenic karst system, developed in well-layered carbonates, comprises horizontal conduits characterized, in vertical sections, by scalloped 2D dissolution profiles.

Our data indicate that the 2D cave vertical profile (i.e., the bedding-parallel dissolution intensity orthogonal to the main horizontal conduits) is related to the spacing, thickness, and mineralogy of bedding-parallel stylolites. These results could contribute to many scientific

4

fields of geoscience related to fluid flow simulations in oil and water reservoirs, as well as ore deposits associated with reactivated stylolites.

2 Geological and karst settings

2.1. Tectonic setting

The Irecê Basin lies within the northern part of the São Francisco Craton (SFC), northeastern Brazil (Almeida et al., 2000) (Fig. 1A). The studied caves are located in the southern portion of the Irecê Basin (Fig. 1B), which includes Neoproterozoic carbonates of the Salitre Formation overlying pelites of the Mesoproterozoic Bebedouro Formation and Mesoproterozoic quartzites of the Chapada Diamantina Group (e.g., Magalhães et al., 2016).

The São Francisco Craton corresponds to a large cratonic area segmented by the Congo Craton during the Pangea breakup in the Late Jurassic and Early Cretaceous (Alkmim and Martins-Neto, 2012). Within the São Francisco Craton, the Irecê Basin developed due to extensional tectonics during the fragmentation of the Rodinia supercontinent (c. 950–600 Ma). Normal faults indicate that the extensional regime was active until the sedimentation of the Neoproterozoic basin (D'Angelo et al., 2019).

The Irecê Basin was inverted in the late Brasiliano orogeny (c. 650–500 Ma) (Misi and Veizer, 1998). Most of the contractional deformation is localized within the Riacho do Pontal Mobile to the north of the Irecê Basin (Condie, 2002; Guimarães et al., 2011) and along the contractional quadrant related to the strike-slip fault zones bounding the basin (Cazarin et al., 2021). In the Irecê Basin, the contractional deformation is related to east–west and north-south-verging folds and thrust belts, indicating that two contractional deformation phases usually display a basin-dome pattern (Cruz and Alkmim, 2006; Guimarães et al., 2011; Ennes-Silva et al., 2016; Klimchouk et al., 2016; D'Angelo et al.,

5

129 2019; Balsamo et al., 2020; La Bruna et al., 2020; Pontes et al., 2021). The intensity of

130 contractional deformation decreased southward. Therefore, carbonate units of the Salitre

131 Formation in the southern part of the Irecê Basin display subhorizontal bedding with gentle,

132 high-amplitude folds (Bertotti et al., 2020; La Bruna et al., 2021; Pontes et al., 2021).

133 *2.2. Stratigraphic and speleological settings*

134 The Salitre Formation, which forms the main infill of the Irecê Basin (Fig. 1B),

135 corresponds to a Neoproterozoic ramp deposited on postSturtian Cap carbonate in a gulf-

136 like basin, which overlies the Mesoproterozoic-Neoproterozoic glacial deposits of the

137 Bebedouro Formation (Santana et al., 2021). The Salitre Formation was subjected to

138 dolomitization, silicification, recrystallization and dissolution (Bertotti et al., 2020; Cazarin et

139 al., 2019). The carbonate rocks have been subjected to brittle deformation and intense

140 karstification (Auler and Smart, 2003). Five stratigraphic units host the hypogene cave

141 systems in the northern portion of the Irecê Basin. They are from bottom to top grainstones

142 with cross-bedded stratification, fine grainstones with chert nodules, microbial carbonates,

143 fine siliciclastic layers and marls, and crystalline grainstones interfingered with chert layers

144 (Cazarin et al., 2019).

145 The origin of many caves and dolines concentrated in the southern part of the Irecê

146 Basin is explained by the surrounding mountains of quartzites from the Chapada Diamantina

147 Group. These quartzites generally dip toward the low-elevation domain (center of the basin),

148 correspondent to the carbonates of the Salitre Formation and were the main pathways for

149 the ascending deep-seated fluids. The fluids flowed through the quartzites along the flanks

150 of the hills and entered the carbonate succession, causing extensive karstification (Laureano

151 et al., 2016).

152 *2.3. Cave system*

Karst systems are common in the Salitre Formation. The longest cave system in South America, the Toca da Boa Vista and Toca da Barriguda cave systems, with a total of 140 km of cave passages (Auler et al., 2017), is located in this stratigraphic unit. Both epigenic and hypogenic caves have been described in this unit. The development of hypogenic caves was proposed to be linked to rising hydrothermal fluids ascending and migrating through the fractured basement and were horizontally confined by seals that correspond to low permeable layers (Balsamo et al., 2020; Pisani et al., 2022). The development of caves related to strike-slip fault zones and late silicification of dolostone layers were proposed by Bertotti et al. (2020). The process of karstification was likely enhanced by the oxidation of sulfide-rich rocks in shallow aquifers (Auler and Smart, 2003), a promising scenario that explains the development of a large number of karst systems.

Caves in the Salitre Formation form along fold hinges and associated fracture corridors (Ennes-Silva et al., 2016; La Bruna et al., 2021; Pontes et al., 2020, 2021). Fractures, which provide the main contribution to the secondary porosity of the carbonates from the Salitre Formation, mainly strike parallel to fold hinges (Cazarin et al., 2019). This secondary porosity and high permeability zones facilitated the fluid flow and, consequently, the karstification of cave passages (Bagni et al., 2020; Ennes-Silva et al., 2016; Pontes et al., 2020). The tectonic folds of the Salitre Formation display a basin-dome configuration (Ramsay, 1967), and the maze pattern of the investigated caves contributes to supporting this observation, given that fold hinges are formed in the fold axis and act as flow pathways (Ennes-Silva et al., 2016; Pontes et al., 2021). Finally, Balsamo et al. (2020) highlighted the role of mechanical stratigraphy on the development of multistory karst systems, emphasizing the role of bedding properties (thickness, bed-to-bed interlayers) in determining fracture patterns and permeability anisotropy, thus controlling the shape and main trends of the karstification process of cave systems in the Salitre Formation.

3 Methods

7

179   We used data derived from different methods from the macroscale to the microscale. The analyses include imaging of cave passages by Laser Detecting and Ranging (LiDAR), stratigraphic description of stratigraphic logs in the caves, petrographic analysis of thin sections, porosity and pore-size distribution by mercury-intrusion porosimetry, scanning electron microscopy (SEM), energy dispersive X-ray spectrometry (EDS), and in situ uniaxial compressive strength (UCS) with Schmidt hammer.

185   We have performed a detailed stratigraphic and sedimentary facies description in two stratigraphic logs in Ioio cave and two other stratigraphic logs in Torrinha cave. The mesoscale description of host rocks adopted the Dunham classification of carbonate rocks.

188   The LiDAR survey was performed with the mobile LiDAR system (MLS), developed by a ZEB-Revo GeoSLAM scanner. These data acquisitions aimed to acquire the karst geometry via 3D models. The MLS shows good results in reconstructing cave geometry, but due to its high resolution, we applied the filter Eye-dome lighting from the open-source software Cloud Compare. We selected slices corresponding to the same cave portion, where the stratigraphic logs and sampling were performed. To create 3D models of specific areas, we used the tool "cross-section" on Cloud Compare. In the Torrinha cave, approximately 89 million points were obtained, and 35 million points were obtained in the Ioio cave. In total, we surveyed 1.09 km of cave passages in both caves. To compare the different levels of karstification dissolution, 3D models were made in cave passages. In both caves, the "dissolution intensity" parameter was calculated from 2D slices to compare the different degrees of dissolution between lithological units. To calculate this parameter, a vertical reference line was drawn in the central part of the cave passage. Then, we measured the distance (m) between the reference line and the cave wall in each unit described in the stratigraphic log.

203   We analyzed the petrographic and petrophysical properties that influenced cave development. Fractures were measured in and outside caves, where opening mode I

8

fractures (joints and veins), bed-parallel stylolites and tectonic stylolites occur. The fracture arrangement was analyzed with Stereonet 10.5 open-source stereographic projection software (Allmendinger et al., 2011). The measurements were performed in a direction orthogonal to the main fracture set strike, namely, N–S and E–W, to represent the spatial arrangement of structural features found in the Salitre Formation.

A total of 22 thin sections from each lithostratigraphic unit were analyzed with a Zeiss Axioplan2 standard petrographic microscope. SEM analysis was carried out with a JEOL JSM 6400 SEM equipped with an Oxford-INCA EDS modulus on representative samples to distinguish the chemical composition of rock inside and outside stylolite clusters and evaluate the 2D microporosity. All thin sections were scanned with a Nikon SuperCoolScan 5000 thin section scanner to identify different types of sedimentary and tectonic structures. The high-resolution thickness and spacing of laminations and burial stylolites were measured via ImageJ open-source image analysis software (Schneider et al., 2012).

The porosity and pore-size distribution of the selected and prepared sample amounts were calculated using the Hg-intrusion porosimetry technique with a PoreMaster 33 apparatus (Quantachrome Instruments). A total of 22 samples from both caves were analyzed. The samples were dried at 40 °C for 24 hours in an oven; afterward, ~1.5–2 g of subsamples was inserted into the porosimeter. The measurement settings were as following: sample cell size 1.0 x 3.0 cm, the pressure range was 0.5–33000 psi; the pore size range ranged from 0.0064 to 950 µm; the contact angle of mercury was 140°; and the mercury surface tension was 0.48 N/m (480 dyn/cm). In mercury porosimetry analysis, the applied hydraulic pressure is required to measure the volume of mercury entering porous samples. The pore size distribution data were interpreted using the Washburn equation to calculate the mercury intrusion curves:

$$R = \frac{2\gamma * cos\theta}{P}.$$

where (*P*) corresponds to the hydraulic pressure related to the cross-sectional radius (*R*) of the pore throats accessible by the pressured mercury, together with two material-related thermodynamic parameters, namely, (γ), the surface tension of mercury, and (θ), the contact angle with the sample material (Balsamo et al., 2014; Léon Y León, 1998; Washburn, 1921). The analysis of the intrusion curves was conducted with the software Poremaster 8.01 developed by Quantachrome Instruments. The capillary pressure was obtained from the relation of pressure (psi) with the volume of intruded mercury (%) measured in each sample collected along the stratigraphic logs.

The sample density was calculated with an Ultrapyc 1200E Helium pycnometer (Quantachrome Instruments). The sample density was determined by simply dividing the sample weight (gained with a precision weighing balance) by the measured volume. We provide density as a mean value of 10 consecutive measurements on the same sample.

The procedure we adopted to collect the geomechanical data followed the American Society for Testing Material (ASTM, 2001), in which ten measurements of rebound values were performed for each stratigraphic unit, and the average was calculated to obtain a corresponding value for the unit. The measurements were performed in all sedimentary units of each stratigraphic log using an L-type Schmidt Hammer.

4 Results

The Ioio cave is arranged in a linear pattern, with an absence of recent fluvial sediments (Fig. 2A). The cave displays an alignment of speleothems located in the central portion of the cave conduits, parallel to the cave passages and running along the central part of the cave roof. The study conducted within the Torrinha cave focused on the area displaying the maze pattern and absence of fluvial interference (Fig. 2B). Different lithostratigraphic units that experienced different degrees of dissolution compose the walls of the studied caves. The linear/maze pattern of the passages developed parallel to fractures

10

in an orthogonal pattern expressed on the roof (Pontes et al., 2021). Nonetheless, structural features (e.g., fractures, veins and faults) are rarely observed in the walls, as the karstification process masks them.

The cave geometry and conduits exposed in the study area are characterized by different lithostratigraphic units showing different degrees of karstification, identified by scalloped profiles of vertical cave sections. The scalloped profile of vertical cave sections depends on siliciclastic content, bedding thickness, stylolites, and fractures. The following sections describe the results from LiDAR imagery, field observations, and petrographic and petrophysical analyses. We carefully selected sites that represent all stratigraphic units cropping out in the study area for this study.

4.1 Structural features

The drone imagery shows that both cave entrances developed in doline zones (Fig. 2). The analyzed portion of the Ioio cave corresponds to a N–S-oriented linear conduit (Fig. 2A). The measured bedding indicates that the carbonate strata of the Ioio cave dip to the east and west, forming a gentle and open N–S-oriented anticline. The cave developed chiefly along the anticline fold hinge. Subvertical veins filled with calcite cement striking N–S and NNW–SSE and subvertical stylolites in the ENE–WSW direction were observed (Fig. 2A). A total of 105 fractures were measured inside and outside near the cave entrance (Fig. 2A), displaying fractures orthogonal and parallel to the main N–S cave direction (Fig. 2A).

The Torrinha cave shows a more complex conduit system. Our fieldwork concentrated on the maze section of conduits, a feature common in hypogenic caves. The measured bedding attitude is similar to the Ioio cave, with the primary conduits in their fold hinge. A total of 52 calcite veins strike mostly N–S and E–W, whereas 50 stylolites strike

11

preferentially NNW–SSE (Fig. 2B). Two main trends of fractures, one N–S and the other E–W, were observed, with a subordinate NW–SE trend (Fig. 2B). A total of 270 fractures, 66 veins, 58 stylolites and 217 sedimentary structures (e.g., bedding) were measured in both caves.

4.2 LiDAR survey within the caves

The analyzed portion of the Ioio cave was imaged by LiDAR (Fig. 3A). Within the corresponding cloud point model of the cave, two representative portions were selected (Fig. 3C and D). This portion was selected based on their lithological and vertical relief variations. The same approach was adopted in the Torrinha cave (Fig. 3B, E, F). In total, ~ 1.2 km of karstic conduits were imaged. Our research and sampling were concentrated in stratigraphic logs 1, 2, 3, and 4, respectively, as shown in Fig. 3C, D, E, and F. The surveyed portion of the Ioio cave was localized along the N–S-striking fold axis, resulting in a horizontal linear-cylindrical cave conduit. In Torrinha cave, E–W-striking- and N–S-striking sets parallel to two fold hinges were observed. The main cylindrical conduits are horizontal and are 8-12 m wide. In both cases, the vertical section of horizontal conduits has an elliptical shape with positive and negative relief variations (scalloped profiles in 2D), which follow the lithological variation.

4.3 Stratigraphic and geomechanical logs

The cave analyses indicate different lithostratigraphic units shown in four simplified stratigraphic logs (Fig. 4). Based on the lithological variations, measurements of geomechanical profiles were performed accordingly. Additionally, the dissolution intensity in different units was quantified by measuring the distances from the median line of the cave (starting from the cave apex) to the cave wall in LiDAR imagery and 3D models (Fig. 4).

Stratigraphic log 1, corresponding to site 1 (Fig. 3C) of the Ioio cave, comprises seven lithostratigraphic units. From bottom to top, these units are (1) widely spaced laminated limestone with chert nodules, (2) closely spaced laminated limestone, (3) reddish siltstone, (4) intraformational breccia, (5) limestone with terrigenous content, (6) homogeneous wavy laminated limestone, and (7) intraformational breccia on the top of the gallery. We quantified the uniaxial compressive strength only in the first 3 meters in this portion of the cave (Fig. 5A), with the mean UCS value varying from 44.2 MPa to 57.53 MPa. Stratigraphic log 2 was also performed in the Ioio cave, specifically at site 2 (Fig. 3D). It is composed of 5 lithostratigraphic units, from bottom to top: (1) laminated limestone, (2) closely spaced wavy laminated limestone with terrigenous content on the top, (3) limestone with millimetric siltstone levels, (4) calcarenite limestone with centimetric laminations, and (5) intraformational breccia. The geomechanical profile was made in the first four units (Fig. 5B), with a mean value of 28.84 MPa in unit 1, the lowest mean value and related to a most karstified unit, and 42.95 MPa in unit 3, the less karstified unit in this stratigraphic log.

Stratigraphic log 3 was performed at site 3 in the Torrinha cave (Fig. 3E). The basal unit corresponds to a wavy laminated limestone with a high density of laminations between 0.8 m and 2.10 m and has an intraformational breccia on the top. In addition, we obtained a geomechanical profile along the entire stratigraphic log (Figs. 4 and 5C). The mean value varies from 35.8 MPa in the basal unit to 69.9 MPa and from 49.2 MPa to 62.5 MPa in the top unit. Stratigraphic log 4, related to conduits with a height of 10 m, shows a maze pattern in Torrinha cave (Fig. 3B, F) with the highest unit variation. In total, ten lithostratigraphic units were identified; from bottom to top, these units are (1) laminated limestone, (2) laminated limestone with muddy concretions, (3) wavy laminated limestone, (4) wavy laminated limestone with muddy concretions, (5) densely laminated limestone with silica

13

nodules, (6) teepee, (7) laminated limestone with silica layers and nodules, (8) densely wavy laminated limestone, (9) densely laminated limestone with muddy concretions and calcarenite levels, and (10) densely laminated calcarenite. The UCS values do not show a straightforward relationship with the intensity of dissolution of these lithological units, but in general, in this stratigraphic log, the mean value from less dissolved units is lower than the mean value from most karstified units (Fig. 5D).

Thin section analysis highlights the carbonatic strata arrangement made by millimeter- to centimeter-thick tabular layers that could be classified into three main lithofacies/microfacies, represented by (1) microbial carbonates (Mc), (2) fine siliciclastic/siltstone levels (Sl), and (3) intraformational breccia (Sb). Mc microfacies corresponds to lithologies with a high level of dissolution. The outcrop description shows interbedded and crenulated layers typical of stromatolites. Thin sections present a fine grain matrix (μm to mm size) and allelochemical association – possibly oolites, pellets, and intraclasts (Fig. 6A). The micritization process is intense and difficult to interpret, precisely the alochemical assemblage. Sl and Sb microfacies act as barriers to fluid flow. The fine matrix in the Sl microfacies is characterized by the concentration of terrigenous minerals in stylolite clusters (Fig. 6B). Sb microfacies also behave as a flow barrier due to the poorly selected intraclast grains (cm-size) (Fig. 6C) and the absence of porosity. In general, thin sections do not present significant porosity in Mc. The cementation process, which was active during mesodiagenesis (Choquette and Pray, 1970), reduced the primary porosity of these rocks. The secondary porosity was mostly represented by bedding parallel stylolites and fractures.

4.4 Stylolite spacing and thickness data

Four representative samples, two from the most karstified units and two from the less karstified units, were selected to quantify the spacing and thickness of bedding-parallel laminations (stylolites) visible within the layers (Fig. 7). In both caves, the more dissolved units, represented by the slab samples reported in Figs. 7A and 7C (Ioio and Torrinha caves, respectively), are the units with lower spacing between laminations. Conversely, the units with less dissolution intensity are characterized by greater spacing between laminations, as represented in Figures 7B and 7D. The thickness of laminations, corresponding to stylolite clusters, is greater in most karstified units (Fig. 7A and 7C) than in the less karstified units (Fig. 7B and 7D).

Detailed petrographic analyses were conducted on thin sections from the same representative slab samples (Fig. 8) to (i) quantify the thickness of individual stylolites and (ii) measure the spacing between individual stylolites and between each stylolite within the clusters (Fig. 8C). The lithostratigraphic units with more intense dissolution (Fig. 8A and F) have thicker stylolite clusters, with a mean thickness value of 0.91 mm in the Ioio cave and 1.14 mm in the Torrinha cave (Table 1). The thinner stylolites occur with low amplitude and are isolated as single stylolites (Fig. 8D), with a mean thickness of 0.13 mm in the Ioio cave and 0.23 mm in the Torrinha cave. The spacing between stylolites (individual (Fig. 8E) and clusters) is also directly related to karstification intensity at the microscale. The most karstified units of the Ioio cave have a mean spacing of 2.27 mm, while the less karstified units show a value of 3.51 mm (Table 1). In Torrinha cave, this value is 5.22 mm in the more karstified unit and 10.01 mm in the less karstified unit.

4.5 SEM–EDS analyses and porosity data

SEM analyses were performed on the four samples representing the more dissolved and less dissolved units, highlighting the zones with a high intensity of dissolution (stylolite

15

cluster zones) and zones where the dissolution is less intense in the host rock. The more

karstified units show thicker stylolite clusters (Fig. 9A) and, surprisingly, higher microporosity

inside the clusters with respect to the host rock. To compare the porosity inside the stylolite

cluster zone and within the host rock, we used the SEM images to calculate the 2D porosity

via the image analysis technique. The host rock microporosity varies from 0.68% to 1.33%

in the more dissolved unit and from 1.21% to 1.43% in the less dissolved unit. The

microporosity within the stylolite cluster in the more dissolved unit is 22.22% (Fig. 9A), while

it drops to 11.39% in the less dissolved unit (Fig. 10A). The EDS analysis shows that the

bulk host rock is made of calcite (Fig. 9B) with sparsely distributed dolomitic grains, usually

smaller than 50 μm. The dolomite grains are concentrated within the stylolite cluster,

reaching >90% of the total area (Fig. 9C). Inside the stylolitic cluster, little siliciclastic content

occurs (>3%) (Fig. 9D), as well as minor Fe-oxides and hydroxides (>2%) (Fig. 9E).

The EDS analysis in the less karstified samples shows a composition similar to the

more karstified units, mainly calcite (Fig. 10B) with little detrital dolomite grains. The high-

porosity stylolite is dominantly composed of dolomite (Fig. 10C) with terrigenous accessory

material (Fig. 10D).

4.6 Petrophysical properties of lithological units

Using Hg-intrusion porosity analysis, we measure the total porosity (%), mean pore

size (μm) and capillary pressure of the host rock matrix (n=23 samples). Data are reported

in Table 2 in conjunction with the dissolution intensity of each bed, as measured from LIDAR

2D vertical profiles.

In general, the host-rock matrix porosity of the analyzed samples is low, varying from

1% to 4%. In the samples related to limestones with terrigenous material, the porosity value

16

401 is 18.4%. The values of porosity do not show a clear relation with the degree of karstification

402 and dissolution.

403   For example, in stratigraphic log 2 of Ioio cave, the more karstified unit, corresponding

404 to sample CARB 264, yielded a porosity of 6.46% (Fig. 2, Table 2). The second most

405 dissolved unit has only 1.05%, whereas the less karstified unit has 2.92% total porosity. In

406 Torrinha cave, the most and least karstified unit in stratigraphic log 3 exhibits porosity values

407 of 1.84% and 5.44%, respectively. In stratigraphic log 4, the less karstified unit presents

408 porosity values up to 4.39% (sample CARB 242), whereas the most karstified unit (sample

409 CARB 239) exhibits a porosity of 3.73%. With different degrees of dissolution, all other

410 samples show low values varying from 0.59% to 2.1%.

411   The mean pore size is another petrophysical property with no apparent relation to the

412 degree of dissolution. In stratigraphic log 1, the lowest mean pore size value equals 0.036

413 μm, with all samples showing values lower than 0.9 μm. Only the CARB 262 sample, which

414 corresponds to intraformational breccia, presents values higher than 1, with a mean value

415 of 2.81 μm. Similar values are obtained for stratigraphic logs 2 and 3. In stratigraphic log 4,

416 a wide variation in pore size is observed. Samples CARB 239, CARB 236, and CARB 238

417 present pore sizes of 4.3 μm, 22.71 μm and 20.2 μm, respectively. However, along the same

418 stratigraphic log, samples with low pore size radii were observed (0.14 μm for unit CARB

419 234 and 0.17 μm for unit CARB 241).

420   The capillary pressure, measured in psi, was quantified at 20%, 50%, and 80%

421 thresholds of mercury intrusion volume in each stratigraphic unit (Table 2). As for the

422 porosity and the mean pore size, the pressure values at the mercury volume thresholds do

423 not clearly correlate with the values obtained from the dissolution profile. Sample CARB 257,

424 related to the most karstified unit of column Section 1, until 50% of the mercury intruded

425 volume had no registered pressure, but 279 psi was necessary to obtain 80% of the mercury

intruded volume. On the other hand, the less karstified unit required only 7.82 psi to reach 80% of the volume intruded (Table 2), which sounds counterintuitive.

In stratigraphic log 1 (Table 2), the more dissolved units are those in which the intruded volume of mercury shows a higher percentage in the lower pressure range. Sample CARB 262 shows a different behavior: even if it is part of the less dissolved units, it describes an intrusion curve with more than 70% intruded mercury volume at less than 1 psi. Samples from stratigraphic log 2 (Table 2) that were also collected in the Ioio cave show similar values for all lithological units, with more than 60% of the volume intruded at less than 10 psi.

Samples from stratigraphic log 3 (Table 2), corresponding to the Torrinha cave, show similar values for both less and more karstified units until 10 psi, with approximately 60% of the volume intruded mercury. The variation between the two units occurs in the high-pressure range. In particular, it was necessary to reach 1000 psi to obtain 80% of the volume intruded into the less dissolved unit and approximately 100 psi into the more dissolved unit. Rock samples from stratigraphic log 4 show similar values for all units. Nevertheless, as a general observation, the less dissolved units have a higher intruded volume at lower pressure values than the most dissolved units (Table 2).

4.7. Summary of results

Fig. 11 shows the correlation between all measured petrophysical properties and the dissolution intensity obtained by measuring the scalloped wall profiles in LiDAR images. The diagrams of porosity (Fig. 11A), mean pore size diameter (Fig. 11B), density (Fig. 11C), and capillary pressure (Fig. 11D) indicate that these properties have no clear correlation with the dissolution intensity within the cave conduits.

On the other hand, the stylolite thickness relates to dissolution intensity if compared in each cave. In Torrinha cave, the more karstified units have a mean value of stylolite cluster

thickness of 1.6 mm, whereas the mean thickness of stylolites is 0.28 mm in the less

karstified units (Fig. 11E). In the Ioio cave, this value is 1.38 mm and 0.31 mm in the most

and less karstified units, respectively. Finally, the spacing between laminations clearly

relates to the overall dissolution intensity estimated in both caves (Fig. 11F). The carbonate

units that are more dissolved correspond to lithologies with lower spacing between bedding-

parallel stylolites. The most karstified units from the Ioio cave exhibit a mean spacing

between laminations of 2.62 mm, with the least karstified units having 3.6 mm in the same

cave. Most karstified lithological units in Torrinha cave have a mean spacing of 7.29 mm,

while the least karstified units have a mean value of 15 mm (Fig. 11F). These data suggest

that the spacing of bedding-parallel stylolites (individual or clusters) contained in a bed has

a role in determining the amount of layer dissolution.

5. Discussion

Previous studies highlighted that cave patterns can be determined not only by

lithological differences but can also be related to the vertical distribution and persistence of

fractures (Balsamo et al., 2020; Boersma et al., 2019; Klimchouk, 2007; La Bruna et al.,

2021). In this contribution, we investigated a heterolithic carbonate sequence to constrain

the relationship between karst patterns and the petrophysical/microtextural properties of

lithological units, focusing on the attributes of bedding-parallel stylolites (spacing, thickness).

The stratigraphic logs (Fig. 4) show that both caves were developed within a heterolithic

carbonate package composed of different lithological units. The observed bedding-parallel

laminations occur as submillimeter individual stylolites or cm-thick clusters of stylolites and

are most likely formed during progressive burial estimated to be approximately 1000 m

(Klimchouk et al., 2016). The development of bedding-parallel stylolites in the depth range

of 600–900 m (van Golf-Racht, 1982) reinforces this affirmation.

The stylolite formation process is related to the physical stress-induced compaction of grains along the fluid-filled interface and chemical dissolution, which are partially controlled by the mineralogical heterogeneity of the rock (Bruna et al. 2019). In carbonate reservoirs, stylolites may generate positive porosity and permeability anomalies that guide fluid flow and subsequent dissolution (Araújo et al., 2021; Bruna et al., 2019; Heap et al., 2014; Toussaint et al., 2018). The higher variation in the composition of carbonates from the Salitre Formation explains why some beds exibit a higher number of stylolites than others and therefore different degrees of karstification, since the carbonates do not present primary porosity and are characterized by low values of permeability.

LiDAR imaging is a strong tool for observing variations in 3D cave geometry (e.g., Fabbri et al., 2017; De Waele et al., 2018). The 3D models provided by the LiDAR survey (Fig. 3) were used to constrain the intensity of dissolution from scalloped cave wall profiles and link this parameter with the microtextural and petrophysical properties of lithological units.

5.1 Bedding-parallel stylolites and dissolution intensity

The first-order observation is that siliciclastic units, although more porous, are less dissolved and generally provide the roof of caves. Conversely, limestone lithological units experienced more intense dissolution. This was expected because carbonates are more soluble than clay minerals and quartz-rich rocks (e.g., Flugel, 2010). Another important observation is that most dissolved lithostratigraphic units are densely laminated, with thicker clusters of stylolites varying from 0.91 mm to 1.14 mm (Figs. 7 and 8). In comparison, the thickness of stylolites in units where the dissolution is less intense spans from 0.13 mm to 0.23 mm (Table 1), i.e., one order of magnitude smaller. The spacing between laminations also shows a direct relation with the dissolution intensity of individual beds. The most karstified units show lower spacing between stylolite clusters (Fig. 11E).

499   This can be explained by the fact that although compressional structures developed

500   during progressive overburden (with vertical $\sigma1$), stylolites may represent preferential

501   conduits for fluid infiltration and circulation, causing more effective dissolution (e.g., Araújo

502   et al., 2021). Fluid pathways mostly depend on the interaction between hydrological

503   properties, stratigraphy, and fracture distributions (Odling et al., 1999), which provide

504   connectivity to fluid circulation. In the study caves, which are composed of limestones with

505   low matrix porosity and permeability, the fluid pathways were focused within stylolites

506   parallel to bedding. This is confirmed by the microporosity documented within the stylolite

507   clusters in SEM–EDS images (Figs. 9A and 10A). For example, Kang et al. (2019) affirmed

508   that higher porosity could accelerate the flow and, therefore, the permeability after analyzing

509   the impact of laminar flow. Our data show that the total host-rock matrix porosity is not

510   directly related to the karst dissolution intensity. Nonetheless, 2D porosity analysis

511   conducted in SEM images shows that the porosity along the stylolitic zones is 10-20 times

512   higher than that surrounding the host rock (Figs. 9 and 10), thus supporting the interpretation

513   that such mm- to cm-thick zones can focus fluid flow enhancing dissolution. The porosity

514   values within stylolites documented in this study are surprisingly high, as stylolites consist

515   of concentrated detrital dolomite grains rather than insoluble clay material.

516

5.2 Kast and petrophysical properties

518   The UCS measurements parallel to the bedding are prone to be dissipated by the

519   anisotropy between layers, which act as mechanical discontinuity surfaces (Özbek, 2009).

520   It stands to reason that stratigraphic units with several closely spaced layers should have

521   lower UCS values due to the high anisotropy. Nonetheless, the UCS values we measured

522   indicate that dissolution is not related to the uniaxial strength of carbonates (Fig. 4). In the

523   study area, the only clear relationship with dissolution is provided by the spacing between

laminations and the thickness of stylolitic clusters. Baud et al. (2016) conducted numerical simulations suggesting that rock weakening induced by stylolites is mostly due to the higher porosity and heterogeneity inside and outside the stylolites. These stylolites may act as planes of weakness when the thickness exceeds 5 mm. This value of 5 mm is higher than the mean observed values in our analysis, 0.13 mm to 1.14 mm, respectively, and supports the lack of relation between UCS and dissolution.

The matrix porosity values of the host rock, measured by mercury-intrusion porosimetry (spanning from 0.5% to <5% - Table 2) and capillary pressure/pore size distribution analyses and density (Table 2, Fig. 10 A, B, C), do not display a clear relationship with the dissolution intensity. This could be related to a limited connection between micropores and, therefore, a hampered fluid circulation.

The studied carbonates show a vast variety of pore sizes. This variation is directly related to the complex pattern and to the polymodal pore-size distribution of the curves expressed by pressure (psi) vs. mercury intruded volume (Fig. 10). Therefore, it was difficult to define the exact inflection point of the intrusion curve. Therefore, we compared the pressure needed in different units to obtain the same value of intruded mercury volume. Several studies related the higher capillary pressure to units that act efficiently as sealing and leading the fluid flow (Torabi et al., 2013; Xiong et al., 2015). Even with this relation reported in the literature, a direct relationship with the dissolution intensity comparing the pressure needed to intrude the mercury inside the samples was not observed.

5.3 Stylolites as preferential flow pathways

Several previous contributions have pointed out the role of stylolites acting as barriers or as conduits to fluid flow. The hydraulic barrier role is further enhanced when enrichment of phyllosilicates or calcite precipitation locally occurs within the stylolite zone, closing pore

22

space and hampering fluid flow. However, an increasing number of recent studies have been relating stylolites with fluid flow conduits. These studies observed a high porosity zone surrounding stylolites compared to the host rock. Our case study showed that the more karstified beds have a greater number of thick stylolite clusters (Figs. 7 and 8). Based on EDS images and XRD analysis, we noted that the stylolite cluster zones have greater porosity than the host rock (up to 20% versus <2%). Certainly, these zones of high porosity may act as preferential fluid pathways that increase the dissolution of the surrounding carbonate host rock matrix. In a well-layered heterolithic carbonate sequence, this process ends up with typical scalloped cave profiles.

Our analysis shows that the stylolite clusters are composed of 90% detrital dolomite grains with clayish residual material, terrigenous grains, and Fe oxides as accessory minerals (Figs. 9 and 10). The host rock is made of micritic limestone with minor dolomite grains dispersed into the calcite matrix (Figs. 9 and 10). We suggest that the dissolution in the stylolitic zones has completely removed the $CaCO_3$ and concentrated dolomite grains within the stylolites as a dissolution residue. Our interpretation is supported by Toussaint, who discussed the influence of stylolites as conduits for promoting a permeability path parallel to the stylolites. For example, Riegel et al. (2019) accounted for a relation of microfractures improving the permeability in the matrix and acting as fluid conduits. Here, stylolite clusters acted as "open microfractures", improving the porosity and permeability of the carbonate rock.

5.4 Conceptaul model

Figure 12 summarizes the structural evolution of the Salitre carbonates in the studied cave systems. In the first stage (Fig. 12A), different units were deposited in a bed parallel pattern, and background fractures may have developed. In this phase, bedding-parallel stylolites developed during progressive burial, but no significant dissolution occurred since

23

no connection between the fractures was established. Successive contractional tectonic events caused gentle folding of carbonates from the Salitre Formation in the Irecê Basin. These superposed folding events created clustered fractures in a pattern parallel to the fold hinges (Fig. 12B) and provided fluid pathways increasing fluid circulations (Fig. 12C).

The second stage of cave development occurred following the fluid circulations at different levels affecting the several studied lithological units. The carbonate beds with extensive stylolites acting as microfluid pathways enhanced the karstification process (Fig. 13B). The third stage comprises the last phase of dissolution, resulting in the present-day cave geometry (Fig. 13C) on the cave walls. The geometry is associated with alternating layers showing differential dissolution intensity. In particular, less dissolved layers (Fig. 7B, 7D) composed of limestones with minor siliciclastic content and absence or high spacing between laminations form a positive relief (Fig. 13C). Negative dissolution relief is related to the most dissolved layers, composed of highly laminated limestones (Fig. 7A, 7C) with the extensive occurrence of stylolite clusters (Fig. 8A; 13C). The study by Araujo et al. (2021), who observed a similar process in epigenetic karst in carbonate sequences, further supports our work hypothesis. Several studies have shown that the stratigraphy, fracture pattern, hydrologic setting and preferential orientation of major tectonic discontinuities play a primary role in karst geometry. In this work, we show that minor structures such as burial stylolites also provide key features that may control the hypogenic cave geometry.

6. Conclusion

The present research combines field and laboratory analyses to identify the hypogenic karst geometry and its relationship with petrographic, petrophysical and geomechanical features of Neoproterozoic carbonate rocks of the Salitre Formation, São Francisco Craton, Brazil. The hypogenic caves exhibit alternating positive and negative

24

reliefs on cave sections with different degrees of karstification. Karstification initiated with the entrance of fluids into the carbonate system along N–S- and E–W-striking fractures parallel to fold hinges. These fractures acted as primary flow pathways. The secondary flow pathways were stylolite clusters, which allowed lateral flow, enhancing karstification along the bedding. The major results of this research are summarized below:

- Lithostratigraphic units composed of mixed carbonate and terrigenous grains show lower dissolution intensity than pure limestones. The carbonate chemical composition is therefore directly related to the intensity of karstification.

- Bedding-parallel stylolites in dolomitic limestone consist of high-porosity (up to 20%) mm- to cm-thick zones with >90% dolomite detrital grains.

- As a result, beds with closely spaced and thicker stylolites are more karstified and dissolved, indicating that stylolitic zones act as flow pathways in low porosity-permeability carbonates.

- The new finding of this paper is that the attributes of burial-related stylolites may control cave passage enlargement via selective karstification and bed dissolution.

Acknowledgment

References

Agar, S.M., Geiger, S., 2015. Fundamental controls on fluid flow in carbonates: Current workflows to emerging technologies. Geol. Soc. Spec. Publ. 406, 1–59. https://doi.org/10.1144/SP406.18

Alkmim, F.F., Martins-Neto, M.A., 2012. Proterozoic first-order sedimentary sequences of the São Francisco craton, eastern Brazil. Mar. Pet. Geol. 33, 127–139. https://doi.org/10.1016/j.marpetgeo.2011.08.011

Allmendinger, R.W., Cardozo, N., Fisher, D.M., 2011. Structural geology algorithms: Vectors and tensors, Structural Geology Algorithms: Vectors and Tensors. https://doi.org/10.1017/CBO9780511920202

Almeida, F.F.M. De, Brito Neves, B.B. De, Dal Ré Carneiro, C., 2000. The origin and evolution of the South American platform. Earth Sci. Rev. 50, 77–111. https://doi.org/10.1016/S0012-8252(99)00072-0

Antonellini, M., Nannoni, A., Vigna, B., De Waele, J., 2019. Structural control on karst water circulation and speleogenesis in a lithological contact zone: The Bossea cave system (Western Alps, Italy). Geomorphology 345, 106832. https://doi.org/10.1016/j.geomorph.2019.07.019

Araújo, R.E.B., La Bruna, V., Rustichelli, A., Bezerra, F.H.R., Xavier, M.M., Audra, P., Barbosa, J.A., Antonino, A.C.D., 2021. Structural and sedimentary discontinuities control the generation of karst dissolution cavities in a carbonate sequence, Potiguar Basin, Brazil. Mar. Pet. Geol. 123. https://doi.org/10.1016/j.marpetgeo.2020.104753

ASTM, 2001. ASTM. Standard test method for determination of rock hardness by rebound hammer method. West Conshohocken: ASTM International;

27

668 Audra, P., Palmer, A.N., 2011. Structure des réseaux karstiques : Les contrôles de la

669 spéléogenèse épigène. Geomorphol. Reli. Process. Environ. 359–378.

670 https://doi.org/10.4000/geomorphologie.9571

671 Auler, A.S., Klimchouk, A., Bezerra, F.H.R., Cazarin, C.L., Ennes-Silva, R., Balsamo, F.,

672 2017. Origin and Evolution of Toca da Boa Vista and Toca da Barriguda Cave System

673 in North-eastern Brazil, in: Hypogene Karst Regions and Caves of the World, Cave

674 and Karst Systems of the World. pp. 827–840. https://doi.org/10.1007/978-3-319-

675 53348-3_56

676 Auler, A.S., Smart, P.L., 2003. The influence of bedrock-derived acidity in the development

677 of surface and underground karst: Evidence from the Precambrian carbonates of

678 semi-arid northeastern Brazil. Earth Surf. Process. Landforms 28, 157–168.

679 https://doi.org/10.1002/esp.443

680 Bagni, F.L., Bezerra, F.H., Balsamo, F., Maia, R.P., Dall'Aglio, M., 2020. Karst dissolution

681 along fracture corridors in an anticline hinge, Jandaíra Formation, Brazil: Implications

682 for reservoir quality. Mar. Pet. Geol. 115, 104249.

683 https://doi.org/10.1016/j.marpetgeo.2020.104249

684 Balsamo, F., Bezerra, F.H.R., Klimchouk, A.B., Cazarin, C.L., Auler, A.S., Nogueira, F.C.,

685 Pontes, C., 2020. Influence of fracture stratigraphy on hypogene cave development

686 and fluid flow anisotropy in layered carbonates, NE Brazil. Mar. Pet. Geol. 114,

687 104207. https://doi.org/10.1016/j.marpetgeo.2019.104207

688 Barbier, M., Leprêtre, R., Callot, J.P., Gasparrini, M., Daniel, J.M., Hamon, Y., Lacombe,

689 O., Floquet, M., 2012. Impact of fracture stratigraphy on the paleo-hydrogeology of the

690 Madison Limestone in two basement-involved folds in the Bighorn basin, (Wyoming,

691 USA). Tectonophysics 576–577, 116–132. https://doi.org/10.1016/j.tecto.2012.06.048

28

Baud, P., Rolland, A., Heap, M., Xu, T., Nicolé, M., Ferrand, T., Reuschlé, T., Toussaint, R., Conil, N., 2016. Impact of stylolites on the mechanical strength of limestone. Tectonophysics 690, 4–20. https://doi.org/10.1016/j.tecto.2016.03.004

Bertotti, G., Audra, P., Auler, A.S., Bezerra, F.H.R., de Hoop, S., Pontes, C., Prabhakaran, R., Lima, R., 2020. The Morro Vermelho Hypogenic Karst System: stratigraphy, fractures and flow in a carbonate strike-slip fault zone with implications for carbonate reservoir. Am. Assoc. Pet. Geol. Bull.

Boersma, Q., Prabhakaran, R., Bezerra, F.H., Bertotti, G., 2019. Linking natural fractures to karst cave development: a case study combining drone imagery, a natural cave network and numerical modelling. Pet. Geosci. petgeo2018-151. https://doi.org/10.1144/petgeo2018-151

Bruna, P.O., Lavenu, A.P.C., Matonti, C., Bertotti, G., 2019. Are stylolites fluid-flow efficient features? J. Struct. Geol. 125, 270–277. https://doi.org/10.1016/j.jsg.2018.05.018

Carozzi, A. V., Bergen, D. Von, 1987. Stylolitic Porosity in Carbonates: a Critical Factor for Deep Hydrocarbon Production. J. Pet. Geol. 10, 267–282. https://doi.org/10.1111/j.1747-5457.1987.tb00946.x

Cazarin, C.L., Bezerra, F.H.R., Borghi, L., Santos, R. V., Favoreto, J., Brod, J.A., Auler, A.S., Srivastava, N.K., 2019. The conduit-seal system of hypogene karst in Neoproterozoic carbonates in northeastern Brazil. Mar. Pet. Geol. 101, 90–107. https://doi.org/10.1016/j.marpetgeo.2018.11.046

Condie, K.C., 2002. The supercontinent cycle: Are there two patterns of cyclicity? J. African Earth Sci. 35, 179–183. https://doi.org/10.1016/S0899-5362(02)00005-2

Cruz, S.C.P., Alkmim, F.F., 2006. The tectonic interaction between the Paramirim

aulacogen and the Araçuaí belt, São Francisco craton region, Eastern Brazil. An.

Acad. Bras. Cienc. 78, 151–173. https://doi.org/10.1590/s0001-37652006000100014

D'Angelo, T., Barbosa, M.S.C., Danderfer Filho, A., 2019. Basement controls on cover

deformation in eastern Chapada Diamantina, northern São Francisco Craton, Brazil:

Insights from potential field data. Tectonophysics 772, 228231.

https://doi.org/10.1016/j.tecto.2019.228231

De Waele, J., Fabbri, S., Santagata, T., Chiarini, V., Columbu, A., Pisani, L., 2018.

Geomorphological and speleogenetical observations using terrestrial laser scanning

and 3D photogrammetry in a gypsum cave (Emilia Romagna, N. Italy).

Geomorphology 319, 47–61. https://doi.org/10.1016/j.geomorph.2018.07.012

De Waele, J., Plan, L., Audra, P., 2009. Recent developments in surface and subsurface

karst geomorphology: An introduction. Geomorphology 106, 1–8.

https://doi.org/10.1016/j.geomorph.2008.09.023

Dreybrodt, W., 1990. The role of dissolution kinetics in the development of karst aquifers in

limestone: a model simulation of karst evolution. J. Geol. 98, 639–655.

https://doi.org/10.1086/629431

Dublyansky, Y., 2012. Hydrothermal caves, Second Edi. ed, Encyclopedia of Caves.

Elsevier Inc. https://doi.org/10.1016/B978-0-12-383832-2.00055-4

Ennes-Silva, R.A., Bezerra, F.H.R., Nogueira, F.C.C., Balsamo, F., Klimchouk, A.,

Cazarin, C.L., Auler, A.S., 2016. Superposed folding and associated fracturing

influence hypogene karst development in Neoproterozoic carbonates, São Francisco

Craton, Brazil. Tectonophysics 666, 244–259.

https://doi.org/10.1016/j.tecto.2015.11.006

Fabbri, S., Sauro, F., Santagata, T., Rossi, G., Waele, D., 2017. High-resolution 3-D

mapping using terrestrial laser scanning as a tool for geomorphological and

speleogenetical studies in caves: an example from the Lessini mountains (North Italy).

Geomorphology. https://doi.org/10.1016/j.geomorph.2016.12.001

Flugel, E., 2010. Microfacies of Carbonate Rocks. Analysis, Interpretation and Application,

Second edi. ed, Angewandte Chemie International Edition, 6(11), 951–952. Springer

Heidelberg Dordrecht London New York. https://doi.org/10.1007/10.1007/978-3-642-

03796-2

Gholpoiur, A.M., Cosgrove, J.W., Ala, M., 2016. New theoretical model for predicting and

modelling fractures in folded fractured reservoirs. Pet. Geosci. 22, 257–280.

https://doi.org/10.1144/petgeo2013-055

Gingras, M.K., MacMillan, B., Balcom, B.J., 2002. Visualizing the internal physical

characteristics of carbonate sediments with magnetic resonance imaging and

petrography. Bull. Can. Pet. Geol. 50, 363–369. https://doi.org/10.2113/50.3.363

Gomez-Rivas, E., Martín-Martín, J.D., Bons, P.D., Koehn, D., Griera, A., Travé, A.,

Llorens, M.G., Humphrey, E., Neilson, J., 2022. Stylolites and stylolite networks as

primary controls on the geometry and distribution of carbonate diagenetic alterations.

Mar. Pet. Geol. 136. https://doi.org/10.1016/j.marpetgeo.2021.105444

Guimarães, J.T., Misi, A., Pedreira, A.J., Dominguez, J.M.L., 2011. The Bebedouro

Formation, Una Group, Bahia (Brazil). Geol. Soc. Mem. 36, 503–508.

https://doi.org/10.1144/M36.47

Harris, N.B., 2006. Low-porosity haloes at stylolites in the feldspathic Upper Jurassic Ula

sandstone, Norwegian North Sea: An integrated petrographic and chemical mass-

balance approach. J. Sediment. Res. 76, 444–459.

https://doi.org/10.2110/jsr.2006.040

Heap, M.J., Baud, P., Reuschlé, T., Meredith, P.G., 2014. Stylolites in limestones: Barriers

    to fluid flow? Geology 42, 51–54. https://doi.org/10.1130/G34900.1

Heward, A.P., Chuenbunchom, S., Mäkel, G., Marsland, D., Spring, L., 2000. Nang Nuan

    oil field, B6/27, Gulf of Thailand: Karst reservoirs of meteoric or deep-burial origin?

    Pet. Geosci. 6, 15–27. https://doi.org/10.1144/petgeo.6.1.15

Hosseini, Z., Swennen, R., Mahboubi, A., Moussavi-Harami, R., Mahmudy-Gharaie, M.H.,

    2022. Stylolites (re)activation: A factor in fluid flow and ore emplacement of Irankuh.

    Sediment. Geol. 431. https://doi.org/10.1016/j.sedgeo.2022.106108

Kang, C., Mirbod, P., 2019. Porosity effects in laminar fluid flow near permeable surfaces.

    Phys. Rev. E 100, 1–13. https://doi.org/10.1103/PhysRevE.100.013109

Klimchouk, A., Auler, A.S., Bezerra, F.H.R., Cazarin, C.L., Balsamo, F., Dublyansky, Y.,

    2016. Hypogenic origin, geologic controls and functional organization of a giant cave

    system in Precambrian carbonates, Brazil. Geomorphology 253, 385–405.

    https://doi.org/10.1016/j.geomorph.2015.11.002

Klimchouk, A., Ford, D.C., Palmer, A.N., Dreybrodt, W., 2000. Speleogenesis: Evolution of

    Karst Aquifers. J. Hydrol. 240, 145–146. https://doi.org/10.1016/s0022-

    1694(00)00341-3

Klimchouk, A.B., 2007. Hypogene Speleogenesis: Hydrogeological and Morphogenetic

    Perspective, Special Paper no. 1, second edi. ed. National Cave and Karst Research

    Institute, Carlsbad, NM.

Klimchouk, A.B., Ford, D.C., 2000. Lithologic and structural controls of dissolutional cave

    development. Speleogenes. Evol. Karst Aquifers 54–64.

Koehn, D., Rood, M.P., Beaudoin, N., Chung, P., Bons, P.D., Gomez-Rivas, E., 2016. A

32

new stylolite classification scheme to estimate compaction and local permeability variations. Sediment. Geol. 346, 60–71. https://doi.org/10.1016/j.sedgeo.2016.10.007

La Bruna, V., Bezerra, F.H.R., Souza, V.H.P., Maia, R.P., Auler, A.S., Araujo, R.E.B., Cazarin, C.L., Rodrigues, M.A.F., Vieira, L.C., Sousa, M.O.L., 2021. High-permeability zones in folded and faulted silicified carbonate rocks – Implications for karstified carbonate reservoirs. Mar. Pet. Geol. 128, 105046. https://doi.org/10.1016/j.marpetgeo.2021.105046

Lamarche, J., Lavenu, A.P.C., Gauthier, B.D.M., Guglielmi, Y., Jayet, O., 2012. Relationships between fracture patterns, geodynamics and mechanical stratigraphy in Carbonates (South-East Basin, France). Tectonophysics 581, 231–245. https://doi.org/10.1016/j.tecto.2012.06.042

Laubach, S.E., Olson, J.E., Cross, M.R., 2009. Mechanical and fracture stratigraphy. Am. Assoc. Pet. Geol. Bull. 93, 1413–1426. https://doi.org/10.1306/07270909094

Laureano, F. V., Karmann, I., Granger, D.E., Auler, A.S., Almeida, R.P., Cruz, F.W., Strícks, N.M., Novello, V.F., 2016. Two million years of river and cave aggradation in NE Brazil: Implications for speleogenesis and landscape evolution. Geomorphology 273, 63–77. https://doi.org/10.1016/j.geomorph.2016.08.009

Lyu, X., Zhu, G., Liu, Z., 2020. Well-controlled dynamic hydrocarbon reserves calculation of fracture–cavity karst carbonate reservoirs based on production data analysis. J. Pet. Explor. Prod. Technol. 10, 2401–2410. https://doi.org/10.1007/s13202-020-00881-w

Magalhães, A.J.C., Raja Gabaglia, G.P., Scherer, C.M.S., Bállico, M.B., Guadagnin, F., Bento Freire, E., Silva Born, L.R., Catuneanu, O., 2016. Sequence hierarchy in a Mesoproterozoic interior sag basin: From basin fill to reservoir scale, the Tombador

Formation, Chapada Diamantina Basin, Brazil. Basin Res. 28, 393–432. https://doi.org/10.1111/bre.12117

Misi, A., Veizer, J., 1998. Neoproterozoic carbonate sequences of the Una Group, Irecê Basin, Brazil: chemostratigraphy, age and correlations. Precambrian Res. 89, 87–100. https://doi.org/10.1016/S0301-9268(97)00073-9

Odling, N.E., Gillespie, P., Bourgine, B., Castaing, C., Chilés, J.P., Christensen, N.P., Fillion, E., Genter, A., Olsen, C., Thrane, L., Trice, R., Aarseth, E., Walsh, J.J., Watterson, J., 1999. Variations in fracture system geometry and their implications for fluid flow in fractured hydrocarbon reservoirs. Pet. Geosci. 5, 373–384. https://doi.org/10.1144/petgeo.5.4.373

Ogata, K., Senger, K., Braathen, A., Tveranger, J., 2014. Fracture corridors as seal-bypass systems in siliciclastic reservoir-cap rock successions: Field-based insights from the Jurassic Entrada Formation (SE Utah, USA). J. Struct. Geol. 66, 162–187. https://doi.org/10.1016/j.jsg.2014.05.005

Özbek, A., 2009. Variation of Schmidt hammer values with imbrication direction in clastic sedimentary rocks. Int. J. Rock Mech. Min. Sci. 46, 548–554. https://doi.org/10.1016/j.ijrmms.2008.09.003

Palmer, A., 2016. Groundwater processes in karst terrains. https://doi.org/10.1130/SPE252-p177

Palmer, A.N., 1991. Origin and morphology of limestone caves. Geol. Soc. Am. Bull. 103, 1–21. https://doi.org/10.1130/0016-7606(1991)103<0001:OAMOLC>2.3.CO;2

Palmer, A.N., 1989. Stratigraphic and structural control of cave development and groundwater flow in the Mammoth Cave region, in: Karst Hydrology: Concepts from the Mammoth Cave Area. pp. 293–316.

Petrella, E., Capuano, P., Celico, F., 2007. Unusual behaviour of epikarst in the Acqua dei

    Faggi carbonate aquifer (Southern Italy). Terra Nov. 19, 82–88.

    https://doi.org/10.1111/j.1365-3121.2006.00720.x

Pisani, L., Antonellini, M., Angeli, I.M.D., Waele, J. De, 2021. Structurally controlled

    development of a sulfuric hypogene karst system in a fold-and-thrust belt (Majella

    Massif , Italy). J. Struct. Geol. 145, 104305. https://doi.org/10.1016/j.jsg.2021.104305

Pisani, L., Antonellini, M., Bezerra, F.H.R., Carbone, C., Auler, A.S., Audra, P., La Bruna,

    V., Bertotti, G., Balsamo, F., Pontes, C.C.C., De Waele, J., 2022. Silicification, flow

    pathways, and deep-seated hypogene dissolution controlled by structural and

    stratigraphic variability in a carbonate-siliciclastic sequence (Brazil). Mar. Pet. Geol.

    139, 105611. https://doi.org/10.1016/j.marpetgeo.2022.105611

Pisani, L., Antonellini, M., De Waele, J., 2019. Structural control on epigenic gypsum

    caves: evidences from Messinian evaporites (Northern Apennines, Italy).

    Geomorphology 332, 170–186. https://doi.org/10.1016/j.geomorph.2019.02.016

Pontes, C., Bezerra, F.H., Bertotti, G., Balsamo, F., La, V., Hoop, S. De, 2020. Karst

    conduits formed along fracture corridors in anticline hinges of carbonate units –

    implications for reservoir quality.

Pontes, C.C.C., Bezerra, F.H.R., Bertotti, G., La Bruna, V., Audra, P., De Waele, J., Auler,

    A.S., Balsamo, F., De Hoop, S., Pisani, L., 2021. Flow pathways in multiple-direction

    fold hinges: Implications for fractured and karstified carbonate reservoirs. J. Struct.

    Geol. 146, 104324. https://doi.org/10.1016/j.jsg.2021.104324

Popov, P., Qin, G., Bi, L., Efendiev, Y., Ewing, R., Kang, Z., Li, J., 2007. Multiscale

    methods for modeling fluid flow through naturally fractured carbonate karst reservoirs.

    Proc. - SPE Annu. Tech. Conf. Exhib. 6, 3714–3722. https://doi.org/10.2523/110778-

859 ms

860 Ramsay, J.G., 1967. Folding and Fracturing of Rocks. McGraw-Hill, New York, p. 568.

861 Reis, H.L.S., Gomes, C.J.S., Fragoso, D.G.C., Kuchenbecker, M., 2013. O cinturão

862 epidérmico de antepaís da Bacia de Irecê, Cráton do São Francisco: Principais

863 elementos estruturais e modelagem física analógica. Geol. USP - Ser. Cient. 13, 125–

864 139. https://doi.org/10.5327/Z1519-874X201300040007

865 Riegel, H., Zambrano, M., Balsamo, F., Mattioni, L., Tondi, E., 2019. Petrophysical

866 properties and microstructural analysis of faulted heterolithic packages: A case study

867 from Miocene turbidite successions, Italy. Geofluids 2019.

868 https://doi.org/10.1155/2019/9582359

869 Rustichelli, A., Tondi, E., Korneva, I., Baud, P., Vinciguerra, S., Agosta, F., Reuschlé, T.,

870 Janiseck, J.M., 2015. Bedding-parallel stylolites in shallow-water limestone

871 successions of the Apulian carbonate platform (central-Southern Italy). Ital. J. Geosci.

872 134, 513–534. https://doi.org/10.3301/IJG.2014.35

873 Santana, A., Chemale, F., Scherer, C., Guadagnin, F., Pereira, C., Santos, J.O.S., 2021.

874 Paleogeographic constraints on source area and depositional systems in the

875 Neoproterozoic Irecê Basin, São Francisco Craton. J. South Am. Earth Sci. 109.

876 https://doi.org/10.1016/j.jsames.2021.103330

877 Torabi, A., Fossen, H., Braathen, A., 2013. Insight into petrophysical properties of

878 deformed sandstone reservoirs. Am. Assoc. Pet. Geol. Bull. 97, 619–637.

879 https://doi.org/10.1306/10031212040

880 Toussaint, R., Aharonov, E., Koehn, D., Gratier, J.P., Ebner, M., Baud, P., Rolland, A.,

881 Renard, F., 2018. Stylolites: A review. J. Struct. Geol. 114, 163–195.

882 https://doi.org/10.1016/j.jsg.2018.05.003

36

883 Van Geet, M., Swennen, R., Wevers, M., 2000. Quantitative analysis of reservoir rocks by

884 microfocus X-ray computerised tomography. Sediment. Geol. 132, 25–36.

885 https://doi.org/10.1016/S0037-0738(99)00127-X

886 Wang, X., Lei, Q., Lonergan, L., Jourde, H., Gosselin, O., Cosgrove, J., 2017.

887 Heterogeneous fluid flow in fractured layered carbonates and its implication for

888 generation of incipient karst. Adv. Water Resour. 107, 502–516.

889 https://doi.org/10.1016/j.advwatres.2017.05.016

890 Worthington, S.R.H., Ford, D.C., 1995. High sulfate concentrations in limestone springs :

891 An important factor in conduit initiation ? Environ. Geol. 9–15.

892 Xiong, Y., Winterfeld, P., Wang, C., Huang, Z., Wu, Y.S., 2015. Effect of large capillary

893 pressure on fluid flow and transport in stress-sensitive tight oil reservoirs. Proc. - SPE

894 Annu. Tech. Conf. Exhib. 2015-Janua, 5072–5097. https://doi.org/10.2118/175074-ms

895 Xu, X., Chen, Q., Chu, C., Li, G., 2017. Tectonic evolution and paleokarstification of

896 carbonate rocks in the Paleozoic Tarim Basin. Carbonates and Evaporites 32, 487–

897 496. https://doi.org/10.1007/s13146-016-0307-4
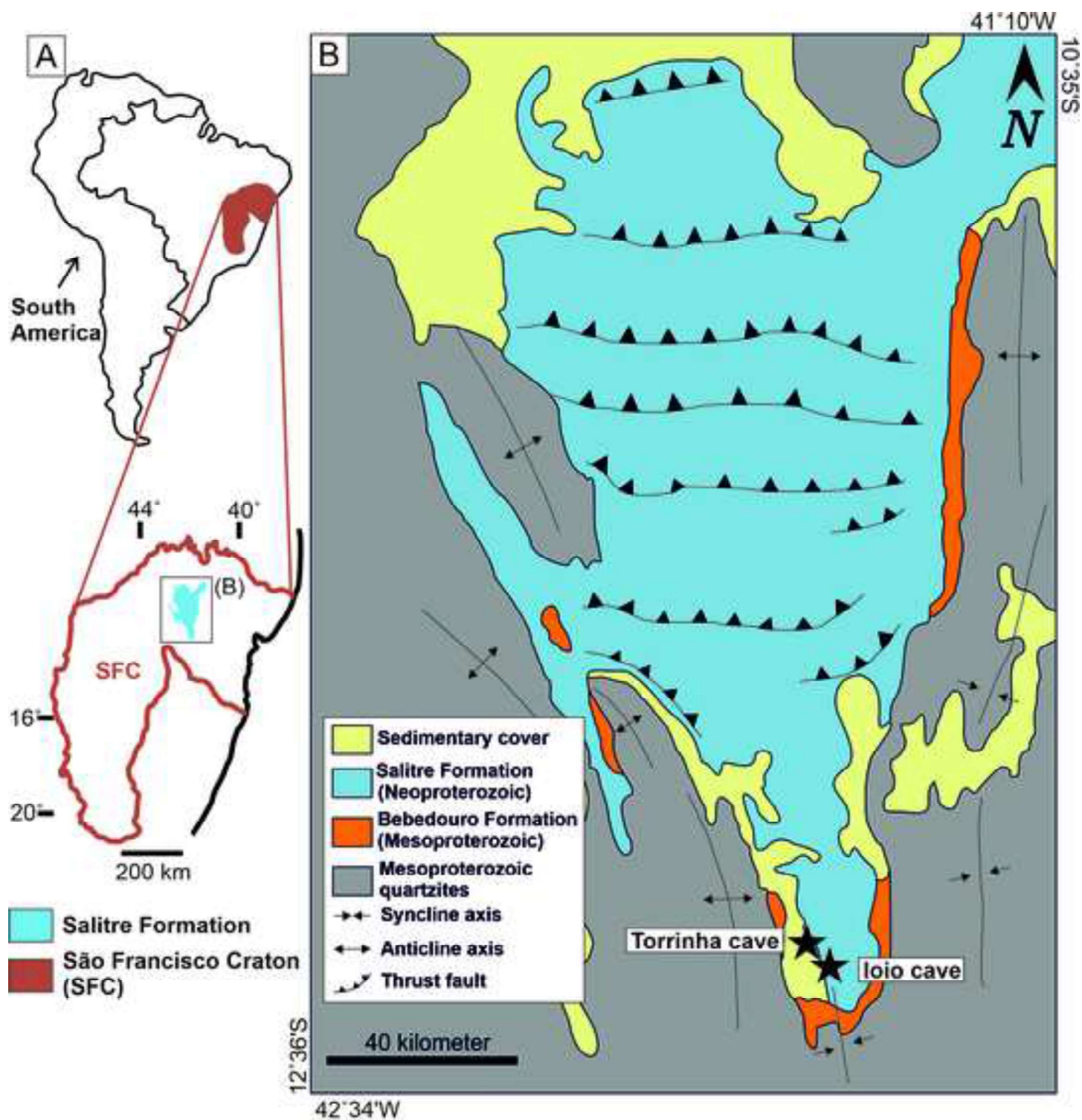
898

899

Figure 1: (A) Sketch map of South America highlighting the São Francisco Craton and the Salitre Formation. (B) Simplified geological map of Irecê Basin with location of studied karstic caves (simplified from Reis et al., 2013).
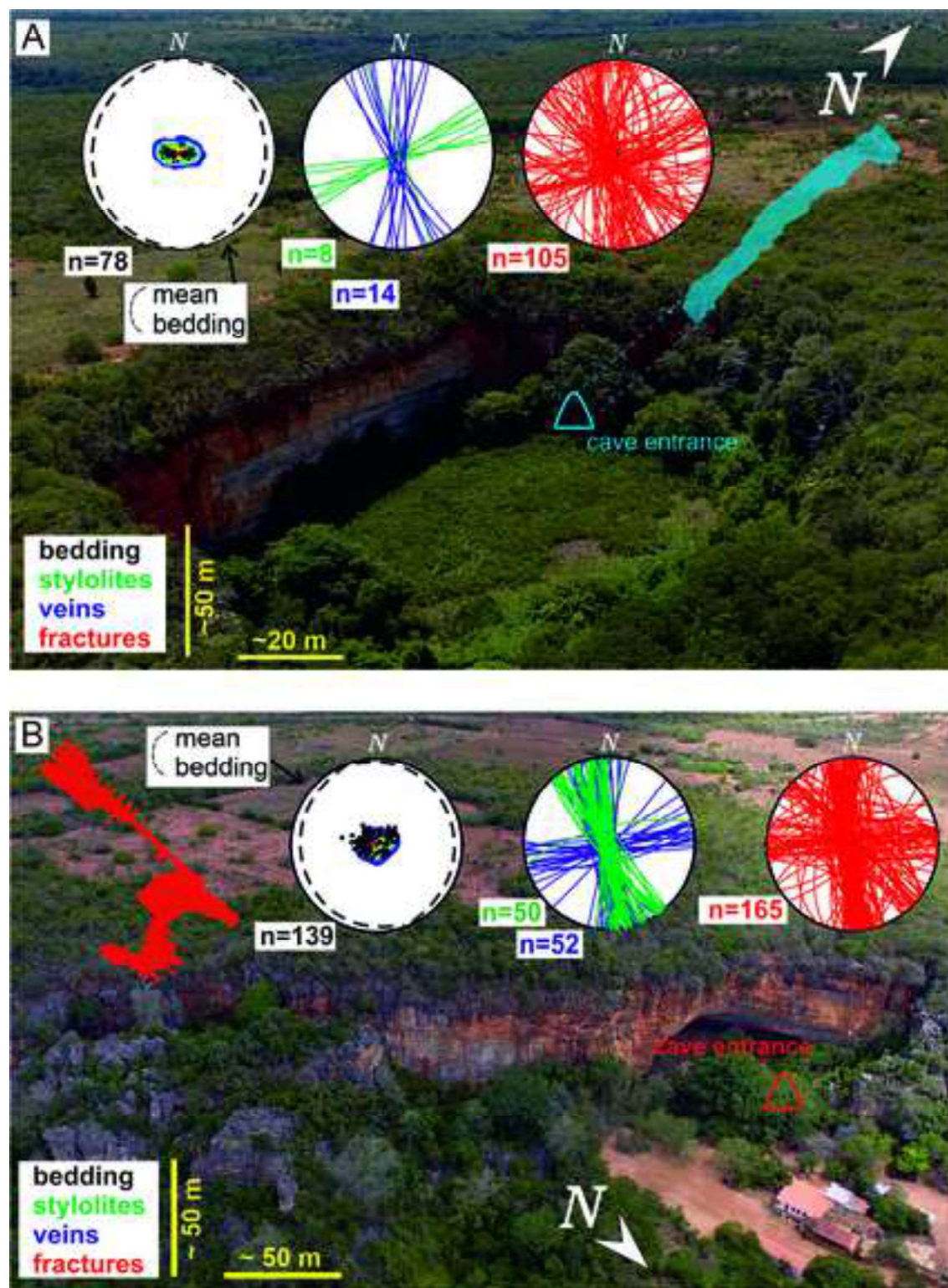
Figure 2   Click here to access/download;Figure;FIGURA 2.jpg ⬇

Figure 2. Drone images show the study areas' morphological features and the structural pattern of caves. (A) Drone image of the Ioio cave entrance and structural data of poles to bedding (black), tectonic stylolites (green), veins (purple) and fractures (red). In light blue a schematic position of an analyzed portion of Ioio cave. (B) Drone image of Torrinha cave entrance and structural data of poles to bedding (black), tectonic stylolites (green), veins (purple) and fractures (red). In light red a schematic position of analyzed portion of Torrinha cave.
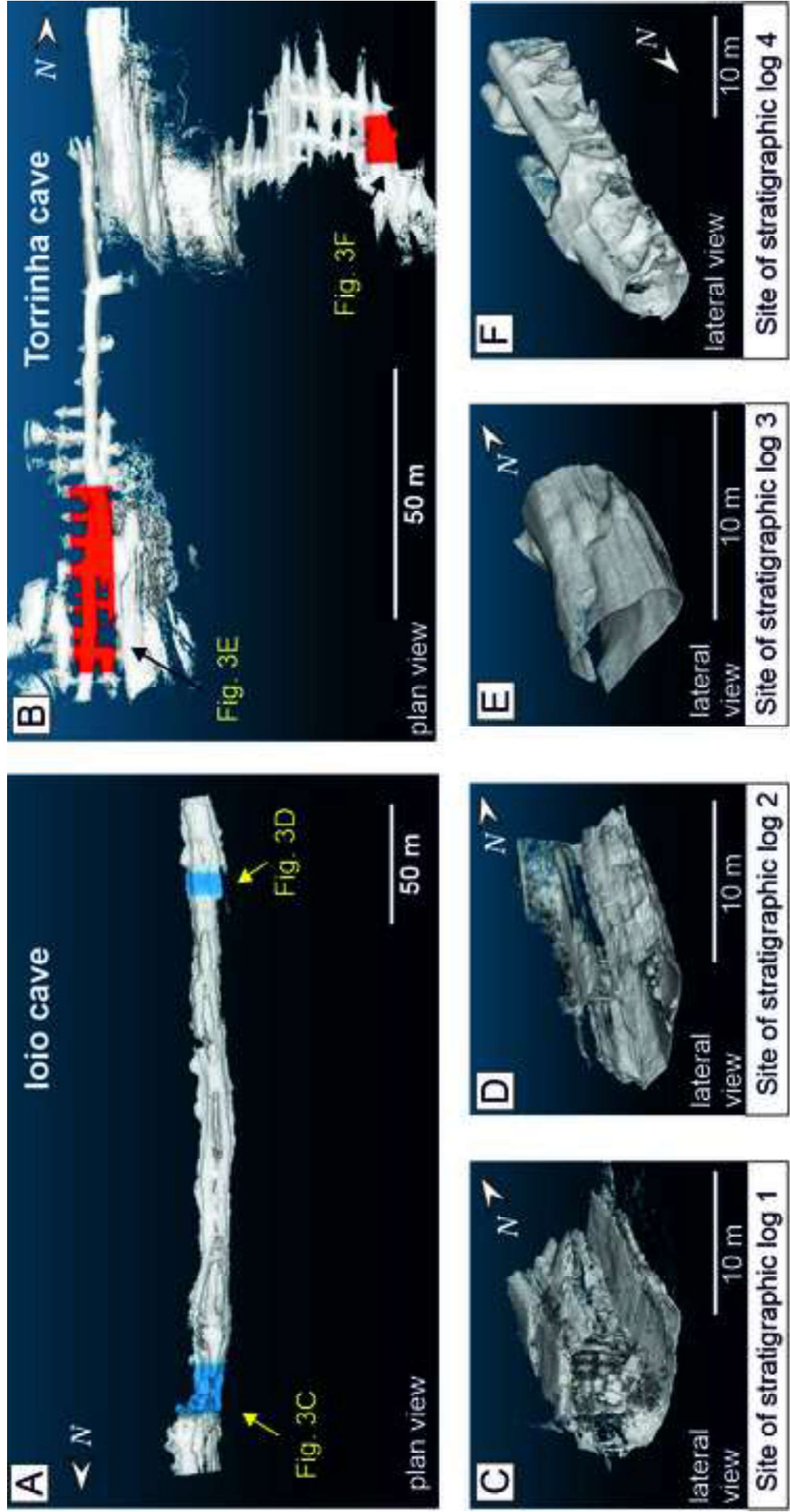
Figure 3

Figure 3: (A) 3D model of the Ioio cave showing the analyzed sites (in blue). (B) 3D model of Torrinha cave showing the analyzed sites (in red). (C) Lateral view of the 3D model in site 1. Site of the stratigraphic log 1. (D) Lateral view of 3D model in site 2. Site of the stratigraphic log 2. (E) Lateral view of 3D model in site 3. Site of the stratigraphic log 3. (F) Lateral view of the 3D model in site 4. Site of the stratigraphic log 4.

Figure 4

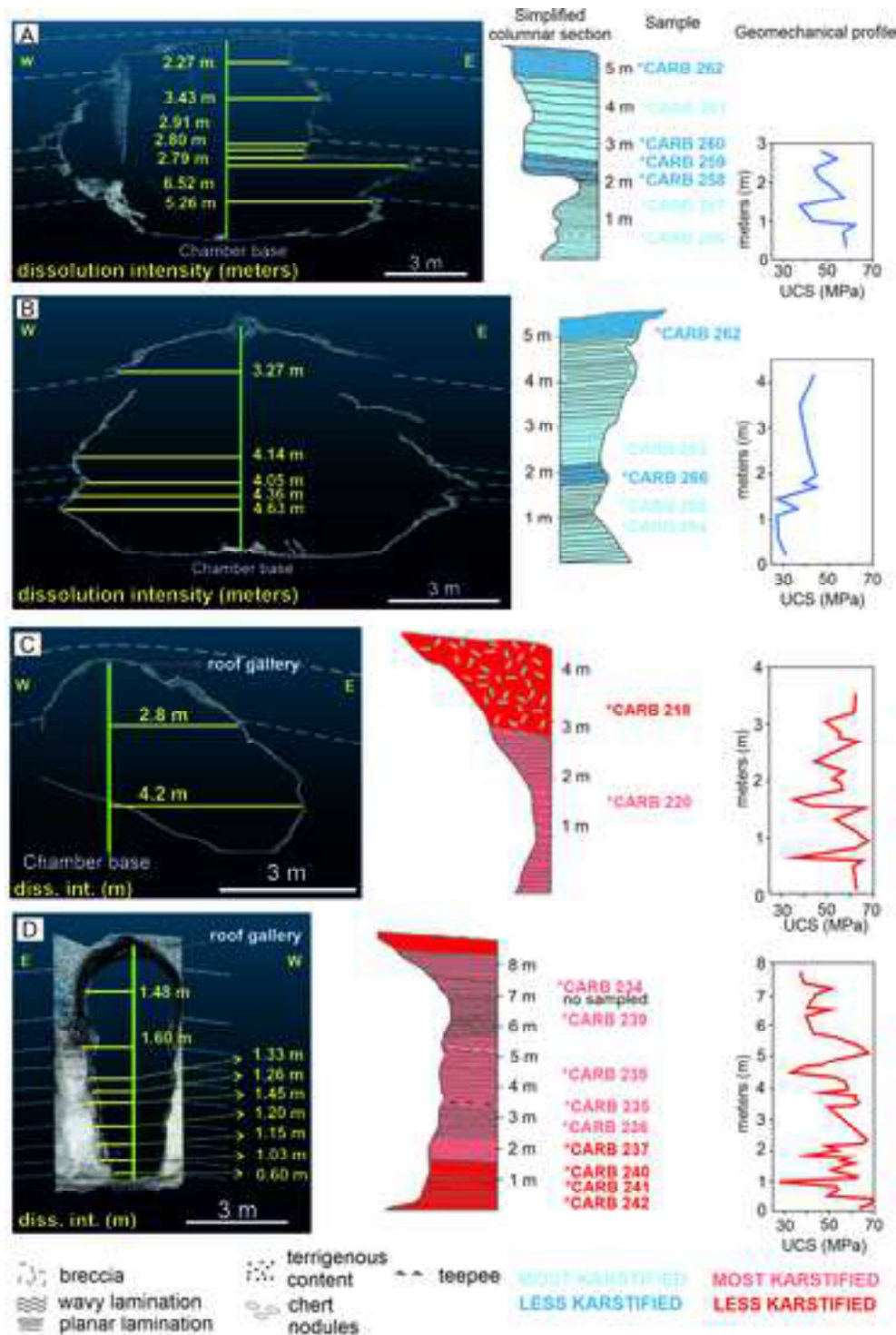Click here to access/download;Figure;figura 4.jpg

Figure 4: Vertical sections of studied cave conduits showing scalloped profiles of walls in conjunction with stratigraphic logs and strength patterns. (A) 3D model slice orthogonal to the analyzed site 1 and its correspondent stratigraphic log, with the most karstified units (blue) and less karstified (light blue). In the middle of the cave, a green reference line marks the position used to measure the dissolution intensity of each unit (light blue horizontal line). (B) 3D model slice orthogonal to the analyzed site 2 and its correspondent stratigraphic log, with the most karstified units (dark blue) and less karstified (light blue). (C) 3D model slice orthogonal to the analyzed site 3 and its correspondent stratigraphic log, with the most karstified units (red) and less karstified (light red). (D) 3D model slice orthogonal to the analyzed site 4 and its correspondent stratigraphic log, with the most karstified units (red) and less karstified (light red).
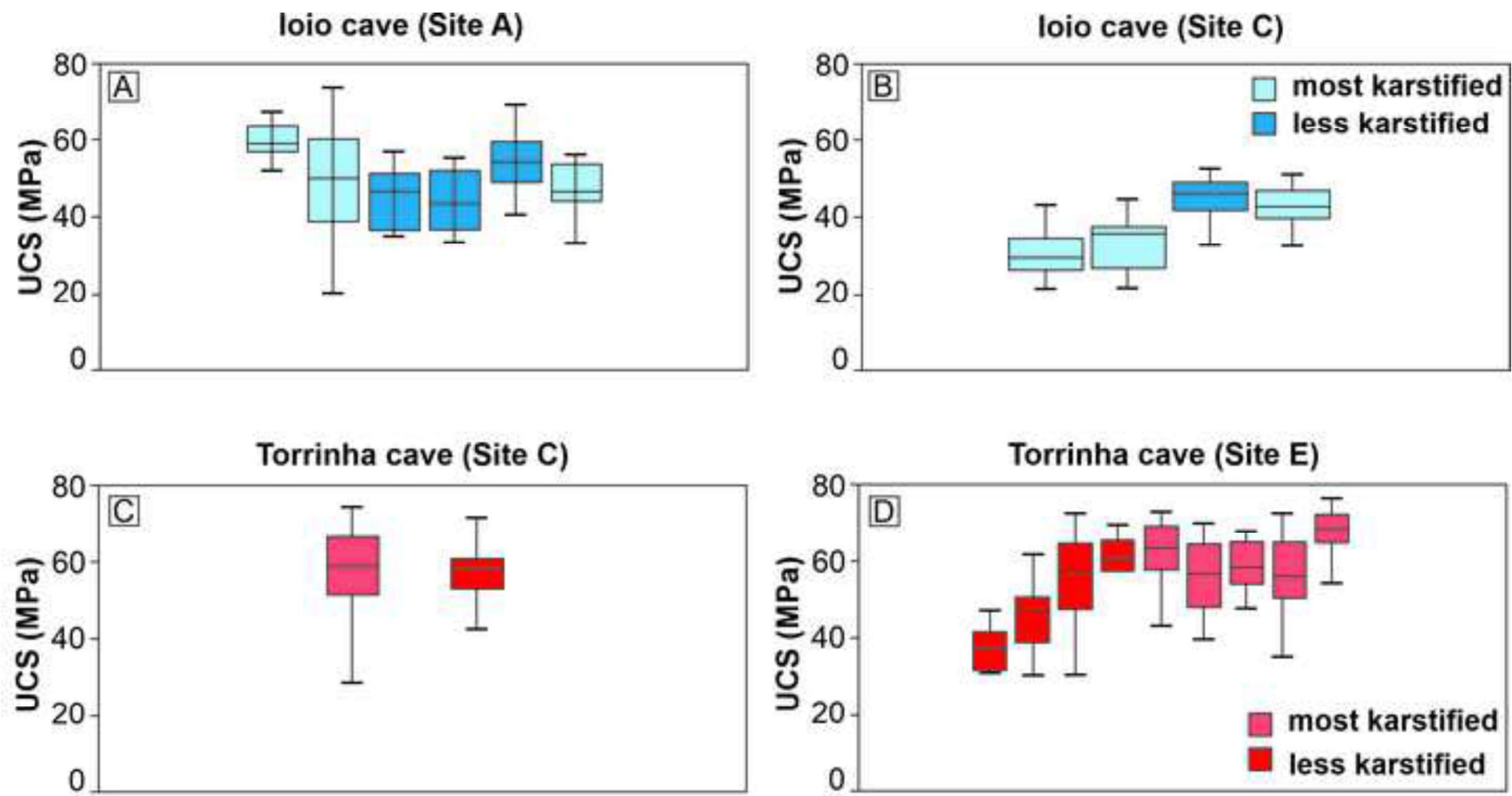
Figure 5

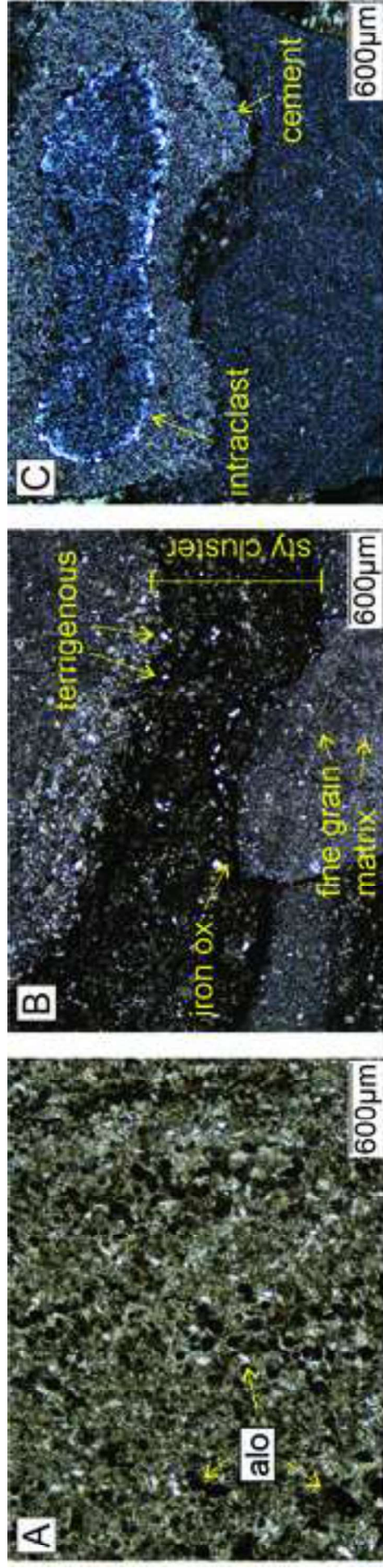Click here to access/download;Figure;Figura 5.jpg ⬇

Figure 5: Uniaxial compressive strength values in each stratigraphic log from (A) site A of Ioio cave, (B) site C of Ioio cave, (C) site C of Torrinha cave and (D) site E of Torrinha cave, highlighting the most karstified and less karstified units.

Figure 6

Figure 6: (A) lithofacies Mc showing the alochemical content. (B) Fine matrix and stylolite (sty) cluster related to the Sl lithofacies. Terrigenous content and iron oxide (ox) are present in the cluster. (C) Facies Sb showing intraclast border embroidered by cement.

Figure 7

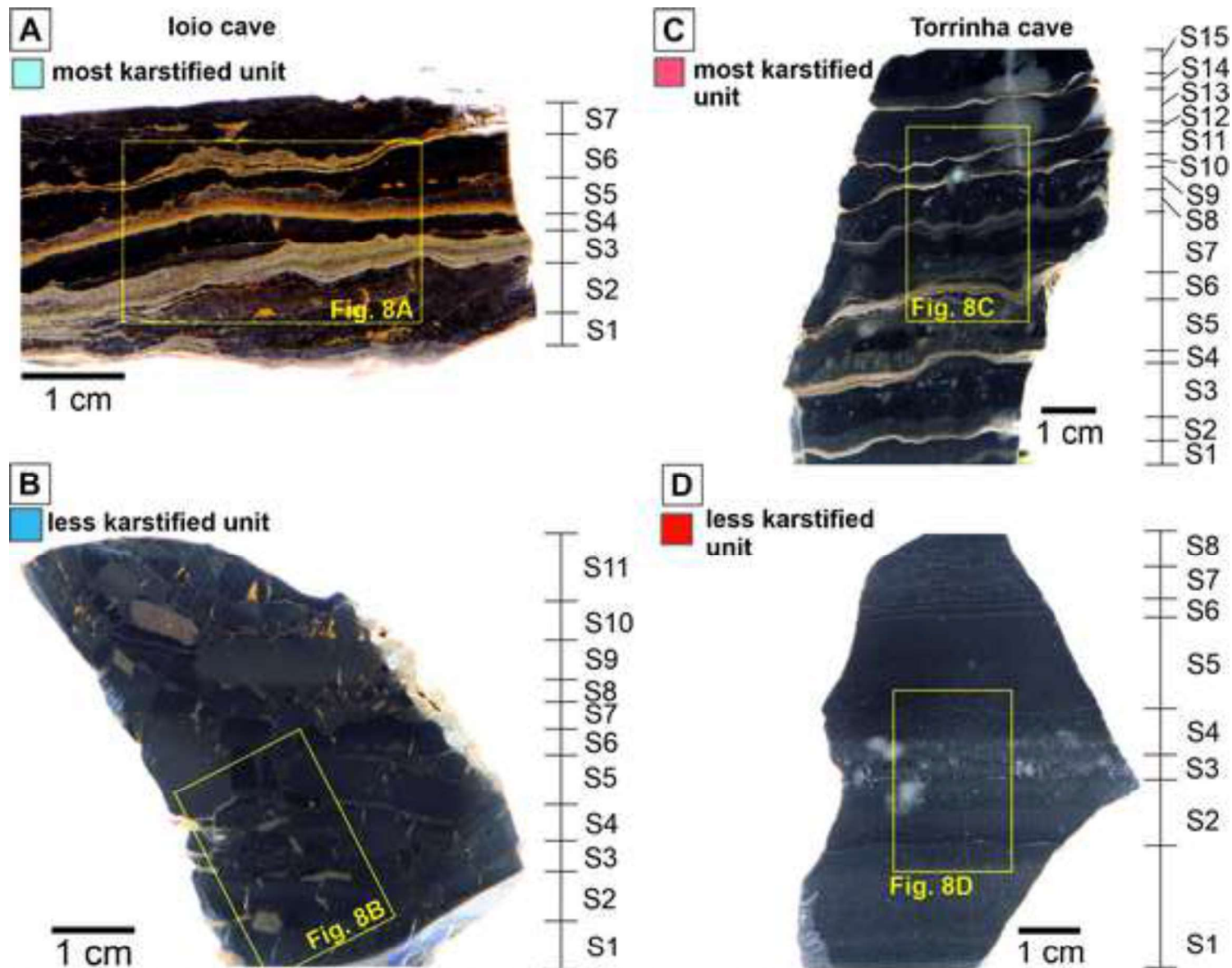Click here to access/download;Figure;fIGURA 7.jpg ±

Figure 7: Representative samples of the (A) more karstified units and (B) less karstified units in the Ioio cave, and (C) more karstified units and (D) less karstified units in Torrinha cave. The yellow rectangles mark the position of thin sections in each sample.
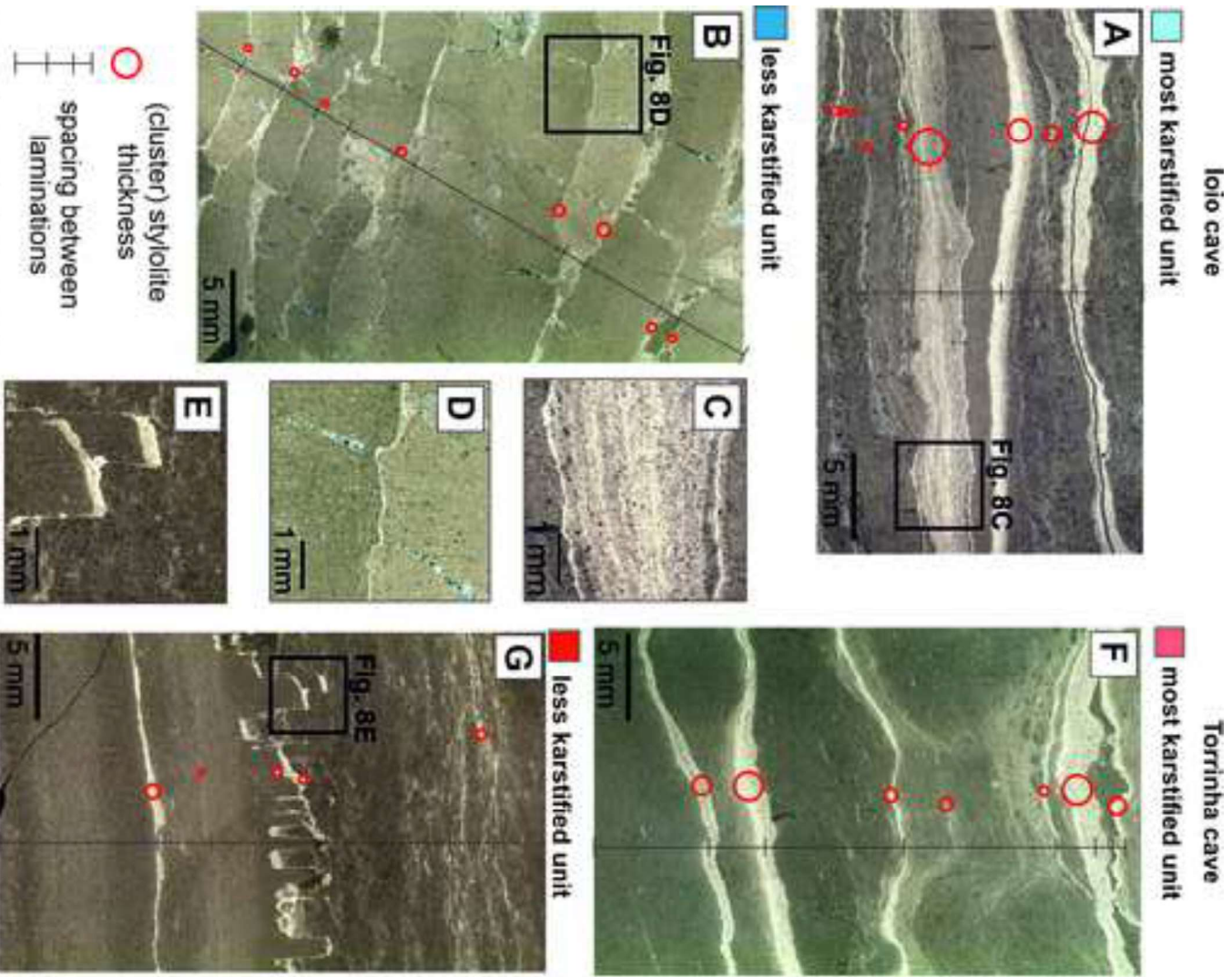
Figure 8

Figure 8: Thin section photomicrographs of representative samples. In (A), most karstified unit with low spacing (S) between laminations and thicker stylolitic clusters (red circle). (B) Intraformational breccia corresponding to the less karstified unit in the Ioio cave. (C) Detail of the stylolite cluster in the most karstified units. (D) Detail of thin stylolite in the less karstified unit. (E) Columnar stylolite seam present in the less karstified unit of the Torrinha cave. (F) Representative sample of the most karstified units in Torrinha cave and (G) less karstified units in Torrinha cave.
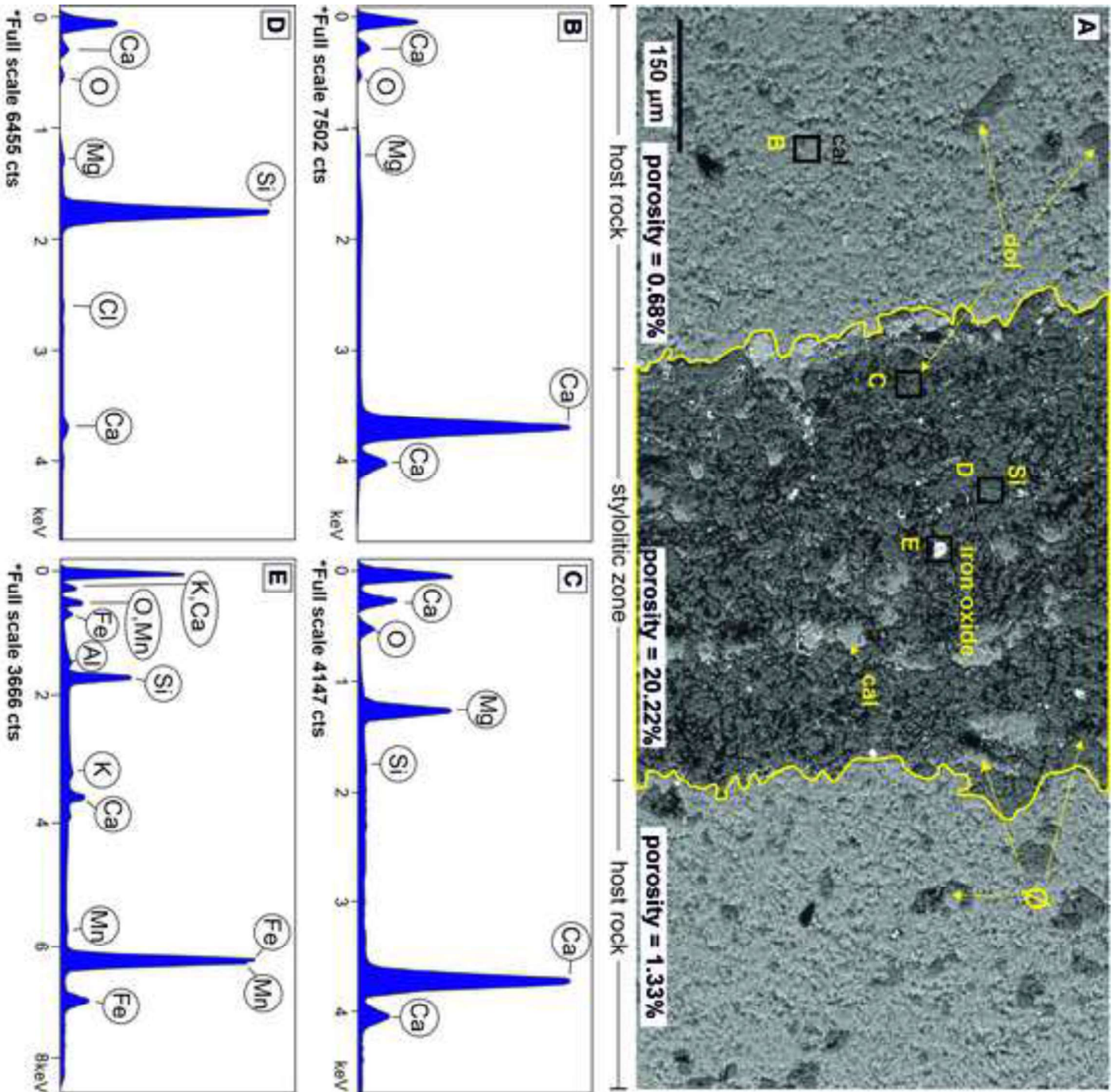
Ioio cave
most karstified unit
less karstified unit

Torrinha cave
most karstified unit
less karstified unit

(cluster) stylolite thickness
spacing between laminations

Figure 9

Figure 9: (A) SEM image showing the detail of a thicker stylolite cluster and related EDS analyzed points, typical of the most dissolved units. (B) X-ray spectrogram from the site B. (C) X-ray spectrogram from the site C. (D) X-ray spectrogram from the site D. (E) X-ray spectrogram from the site E. Key: Cal, calcite; Dol, dolomite; Si, silica; Φ, porosity; Ca, Calcium; O, Oxygen; Fe, Iron; Zn, Zinc; Si, Silica; Al, Aluminum; Mg, Magnesium; K, Potassium; Cl, Chlorine; Mn, Manganese; Mo, Molybdenum.

Figure 10   Click here to access/download;Figure;Figura 10 SEM.jpg ⬇
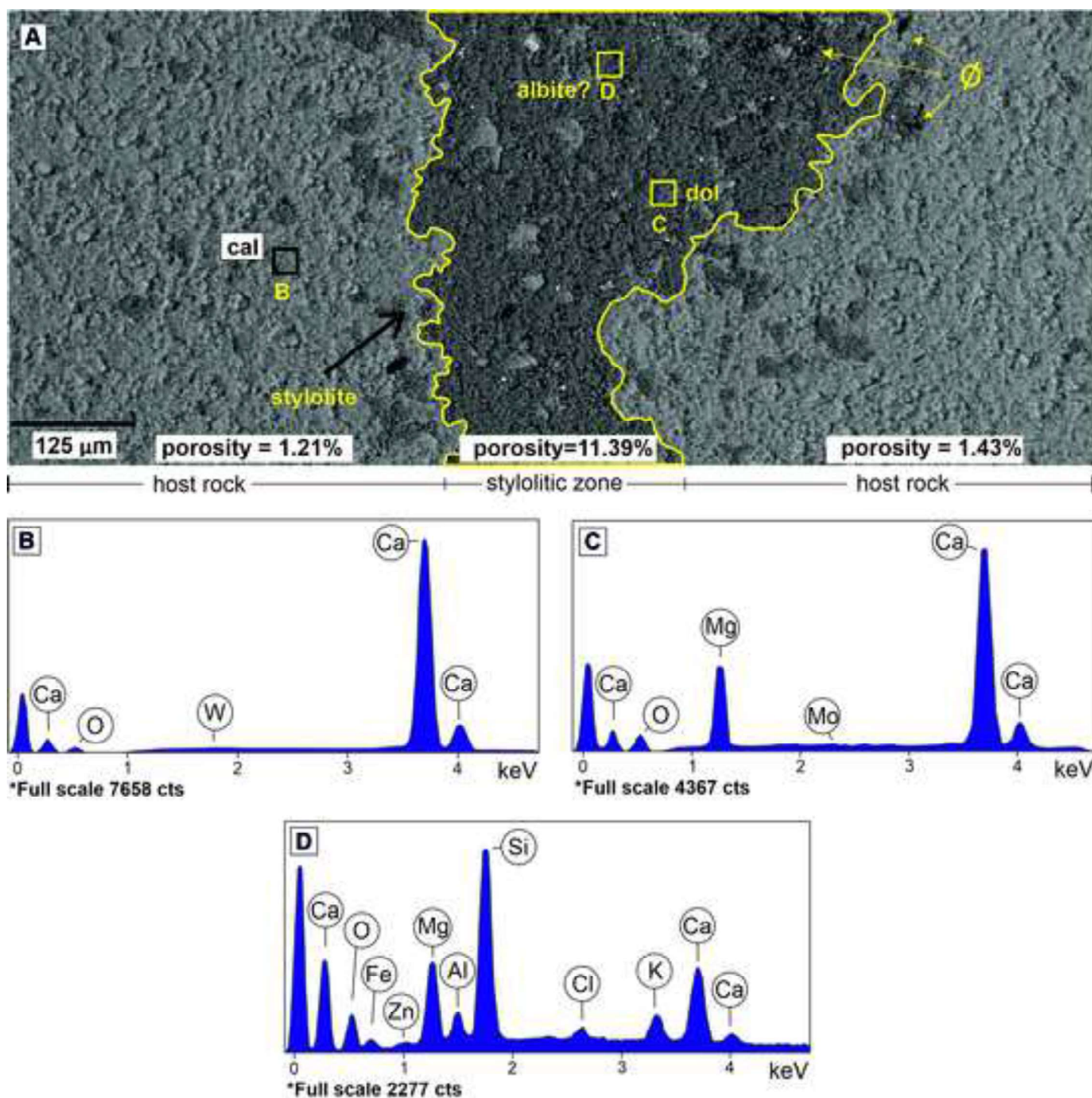

Figure 10: (A) SEM image showing the thicker stylolite cluster associated with EDS analyzed points in the less dissolved units. (B) X-ray spectrogram from the site B. (C) X-ray spectrogram from the site C. (D) X-ray spectrogram from the site D. Dol, dolomite; Φ; porosity Ca, Calcium; O, Oxygen; Fe, Iron; Zn, Zinc; Si, Silica; Al, Aluminum; Mg, Magnesium; K, Potassium; Cl, Chlorine; Mn, Manganese; Mo, Molybdenum.

Figure 11

Click here to access/download;Figure;Figura 11.jpg ⬇

1
2
3
4
5
6
7
8
9
10
11
12
13
14
15
16
17
18
19
20
21
22
23
24
25
26
27
28
29
30
31
32
33
34
35
36
37
38
39
40
41
42
43
44
45
46
47
48
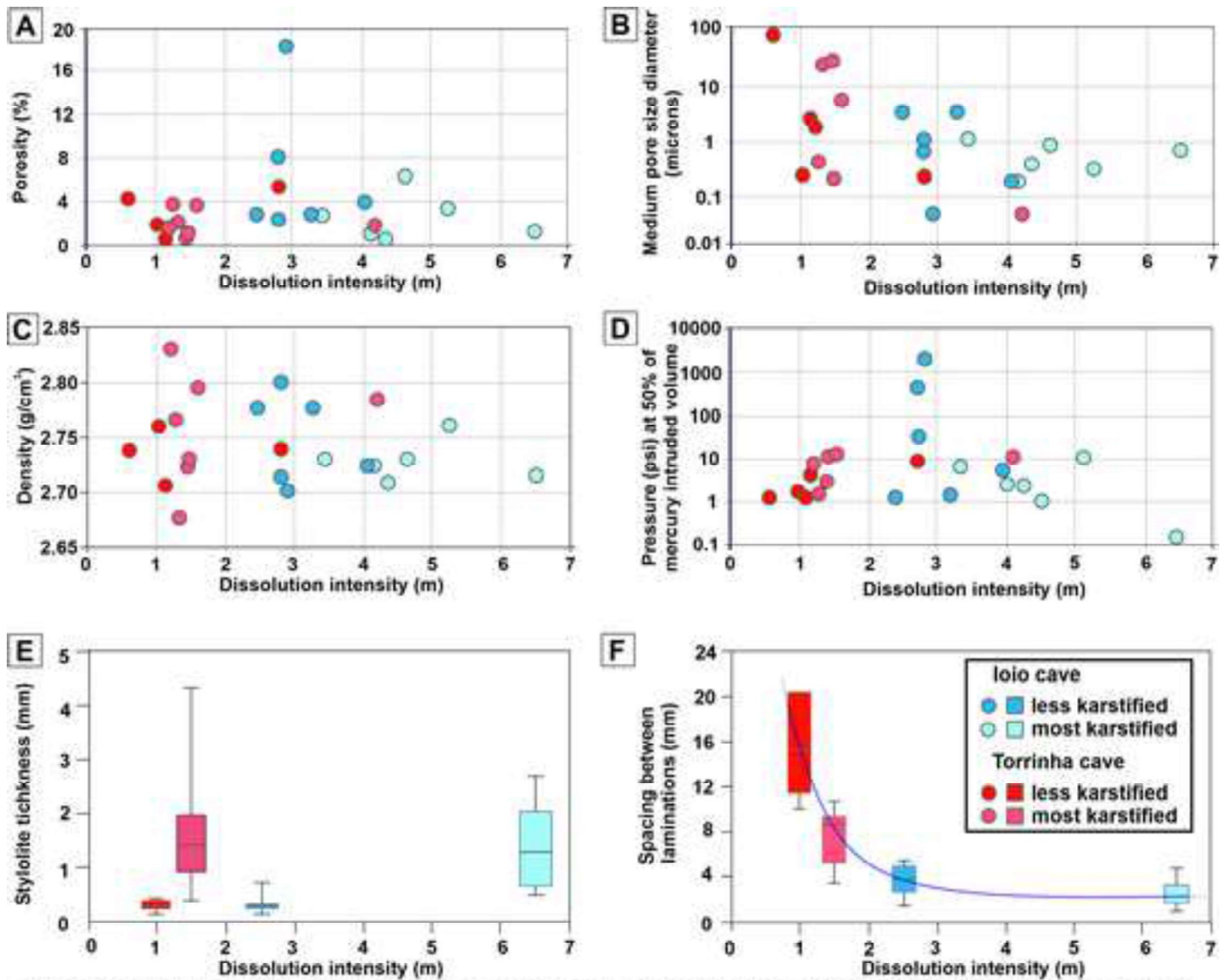49
50
51
52
53
54
55
56
57
58
59
60
61
62
63
64
65

Figure 11: Diagrams of dissolution intensity vs. (A) porosity, (B) mean pore size diameter, (C) density, (D) capillary pressure at 50% of mercury intruded volume, (D) (cluster) stylolite thickness and (E) spacing between laminations.

Figure 12

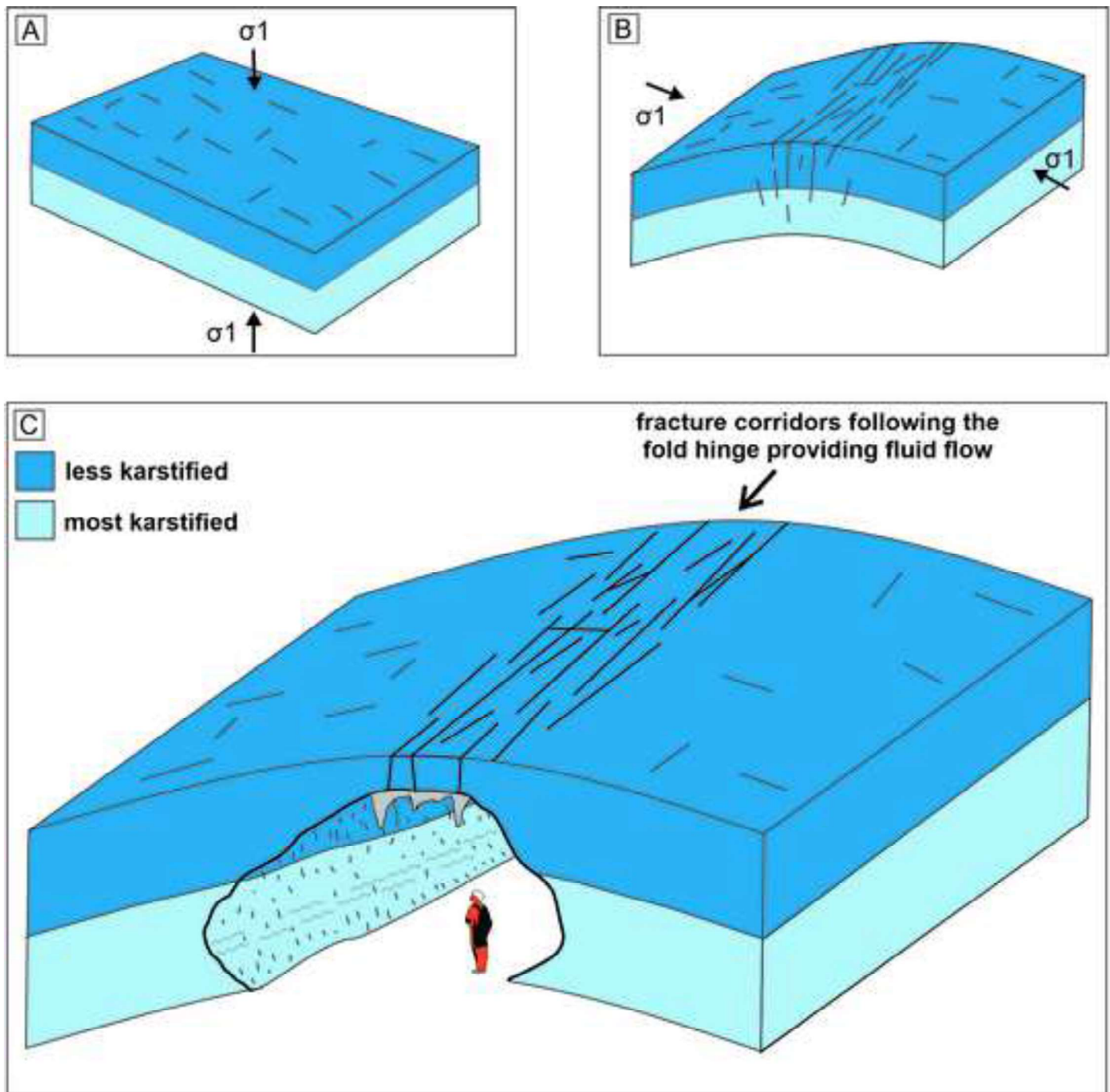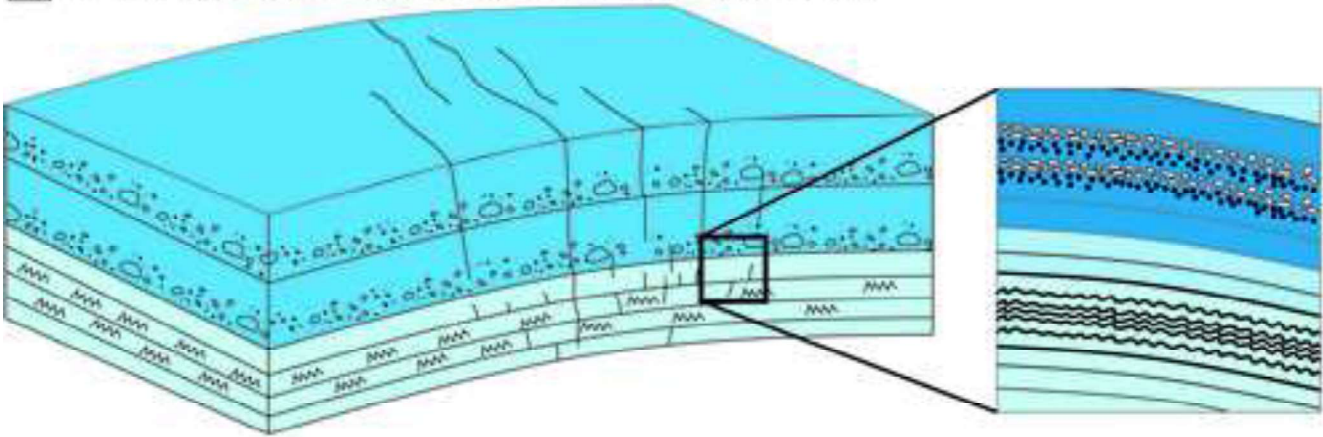Click here to access/download;Figure;figura 12.jpg ⬇

Figure 12: Schematic model of the evolution of fracture corridors along fold hinge, providing flow pathways and enhancing the karstification. Based on Bagni et al. 2020 and Pontes et al. 2020.

Figure 13

Click here to access/download;Figure;Figura 13.jpg ⬇

A first stage: tectonic framework and mineralogical suite

B second stage: fluid flows laterally promoting karstification

fluid flow
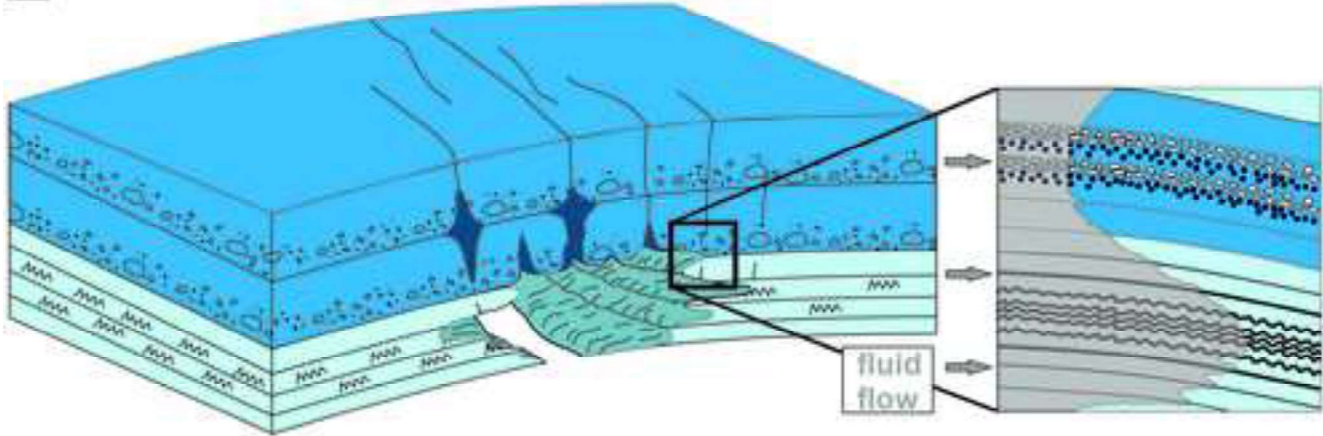
C third stage: differentiated karstified degree (cave geometry)

Geologist as scale

Less karstified

Terrigenous content
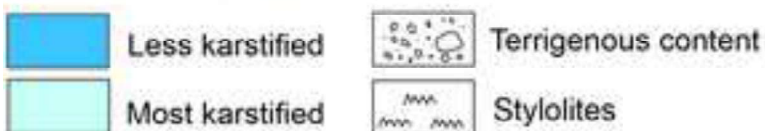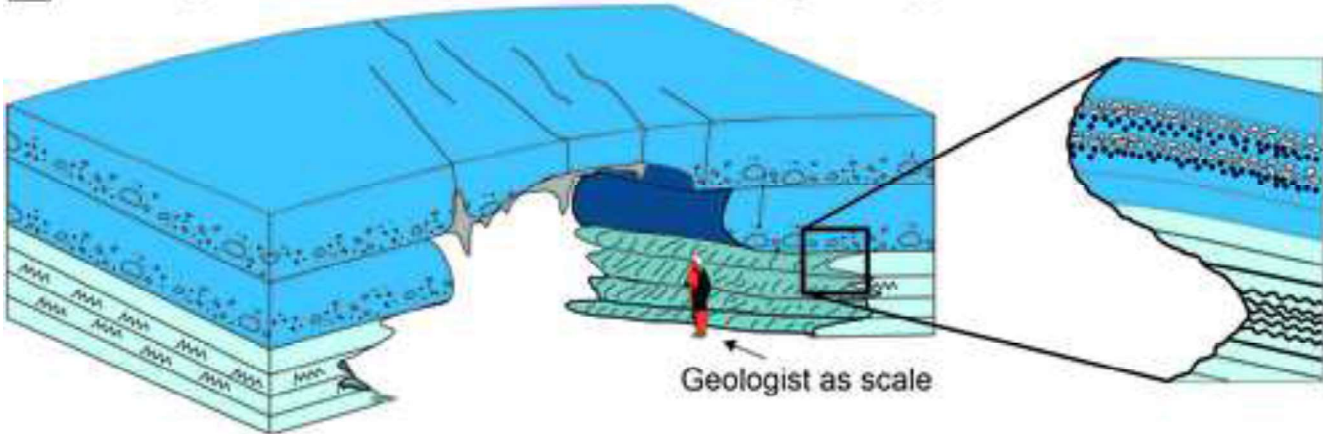
Most karstified

Stylolites

Figure 13: Evolutionary model to explain the cave geometry. (A) Development of preferential discontinuities and tectonic framework in different lithologies. (B) Laterally dissolution/karstification occurs due to the fluid flow along discontinuities. (C) Scalloped profile of cave geometry guided by attributes (thickness and spacing) of burial stylolites.

Table 1

Less karstified - Ioio		Most karstified - Ioio		Less karstified – Torrinha		Most karstified - Torrinha	
Lamination spacing (mm)	Stylolite thickness (mm)	Lamination spacing (mm)	Stylolite thickness (mm)	Lamination spacing (mm)	Stylolite thickness (mm)	Lamination spacing (mm)	Stylolite thickness (mm)
4.2	0.24	1.16	0.29	8.72	0.56	8,24	0.96
3.13	0.32	1.98	0.18	7.15	0.04	3.99	1.68
3.06	0.17	2.12	0.17	14.15	0.44	9.65	1.1
3.35	0.06	1.75	0.41		0.07	3.38	0.98
1.78	0.07	1.76	2.66		0.08	6.98	0.41
5.55	0.15	4.06	1.64			2.4	2.3
2.07	0.05	1.96	0.55			1.91	0.6
4.96	0.06	2.74	2.14				
	0.05	2.86	0.17				
3.51	**0.13**	**2.27**	**0.91**	**10.01**	**0.24**	**5.22**	**1.15**
* medium value in mm.							

Table 1: Measured values in the thin section regarding the spacing (S) between laminations

and stylolite thickness (T).

Table 2

Ioio 01 – Stratigraphic log 1						
sample	dissolution intensity (m)	Porosity (%)	Medium Pore size (microns)	capillary pressure (psi)		
				20%	50%	80% (vol intruded)
264	4,63	6,46	0,6548	1	1	10,29
263	4,14	1,05	0,135	1	2,64	28,17
265	4,36	0,66	0,3043	1,12	2,54	8,6
266	4,05	3,99	0,1314	2,62	5,6	29,5
262	3,27	2,92	2,812	1,03	1,15	7,82
Ioio 02 - Stratigraphic log 2						
sample	dissolution intensity (m)	Porosity (%)	Medium Pore size (microns)	capillary pressure		
				20%	50%	80% (vol intruded)
257	6,52	1,3	0,5213	0	0	279
256	5,26	3,44	0,2381	1,4	10,9	361
261	3,43	2,76	0,8358	1,3	7,14	321
259	2,8	2,35	0,4906	5,9	32,9	276
260	2,91	18,4	0,03627	488	2007	8698
258	2,79	8,19	0,8358	1,46	457	1458
262	2,47	2,92	2,812	1,03	1,15	7,82
Torrinha 01 - Stratigraphic log 3						
sample	dissolution intensity (m)	Porosity (%)	Medium Pore size (microns)	capillary pressure		
				20%	50%	80% (vol intruded)
220	4,2	1,847	0,03489	2,4	11,6	18318,9
218	2,8	5,44	0,1688	2,2	9,6	487,1
Torrinha 02 - Stratigraphic log 4						
sample	dissolution intensity (m)	Porosity (%)	Medium Pore size (microns)	capillary pressure		
				20%	50%	80% (vol intruded)
234	1,48	1,285	0,1462	2,47	11,6	18478
236	1,45	0,758	22,71	1,37	3,01	13,4
238	1,33	2,157	20,2	1,36	1,58	8,96
235	1,26	3851	0,3111	6,6	7,8	527
237	1,2	1,68	1,45	1,58	4,38	15,1
239	1,6	3,736	4,339	11	13,8	23,3
240	1,15	0,596	1,971	0	1,3	22
241	1,03	1,91	0,1737	1,29	1,84	2,74
242	0,6	4,391	86,75	1,27	1,4	1,9

Table 2: Intensity of dissolution (m) and petrophysical properties of total porosity (%), mean pore size distribution (µm) and values of capillary pressure (psi) calculated at thresholds corresponding to 20%, 50% and 80% of mercury intruded volume in the samples collected along the stratigraphic logs.

Declaration of interests

☒ The authors declare that they have no known competing financial interests or personal relationships that could have appeared to influence the work reported in this paper.

☐ The authors declare the following financial interests/personal relationships which may be considered as potential competing interests:

Francisco Hilario Bezerra reports financial support was provided by Shell Brazil Oil.

Authorship contribution statement

Cayo C. Cortez Pontes: Structural data colletion, stratigraphic data colletion, data analysis, conceptualization, writing original draft. Fabrizio Balsamo: Structural data colletion, stratigraphic data colletion, data analysis, conceptualization, Writing – review & editing. Mattia Pizzati: Data analysis, Writing – review & editing. Francisco H. Bezerra: Structural data colletion, conceptualization, funding acquisition, Writing – review & editing. Vincenzo La Bruna: Structural data colletion, stratigraphic data colletion, writing – review & editing. Rebeca S. Lima: Stratigraphic data colletion, data analysis, writing – review & editing.